Supporting Information

Molecularly induced order promotes charge separation through delocalized charge transfer states at donor-acceptor heterojunctions

Xiangkun Jia,‡§[a] Lorenzo Soprani,‡[b] Giacomo Londi,‡[c] Seyed Mehrdad Hosseini,[d] Felix Talnack,[e] Stefan Mannsfeld,[e] Safa Shoaee,[d] Dieter Neher,[d] Sebastian Reineke,[a] Luca Muccioli,[b] Gabriele D'Avino,[f] Koen Vandewal,*[g] David Beljonne,*[c] and Donato Spoltore*[agh]

[a.] Dresden Integrated Center for Applied Physics and Photonic Materials (IAPP) and Institute for Applied Physics, Technische Universität Dresden, 01187 Dresden, Germany.
[b.] Department of Industrial Chemistry "Toso Montanari", University of Bologna, 40136 Bologna, Italy.
[c.] Laboratory for Chemistry of Novel Materials, University of Mons, B-7000 Mons, Belgium. Email: david.beljonne@umons.ac.be
[d.] Institute of Physics and Astronomy, University of Potsdam, Karl-Liebknecht-Str. 24-25, 14476 Potsdam, Germany.
[e.] Center for Advancing Electronics Dresden (cfaed) and Faculty of Electrical and Computer Engineering, Technische Universität Dresden, 01062 Dresden, Germany.
[f.] Grenoble Alpes University, CNRS, Grenoble INP, Institut Néel, 25 rue des Martyrs, 38042 Grenoble, France.
[g.] Institute for Materials Research (IMO-IMOMEC), Hasselt University, Wetenschapspark 1, 3590 Diepenbeek, Belgium. Email: koen.vandewal@uhasselt.be
[h.] Department of Mathematical, Physical and Computer Sciences, University of Parma, V.le delle Scienze 7/A, 43124 Parma, Italy. Email: donato.spoltore@unipr.it
‡ These three authors contributed equally.
§ Present address: Department of Chemical and Biomolecular Engineering, National University of Singapore, 4 Engineering Drive 4, Singapore 117585, Singapore.
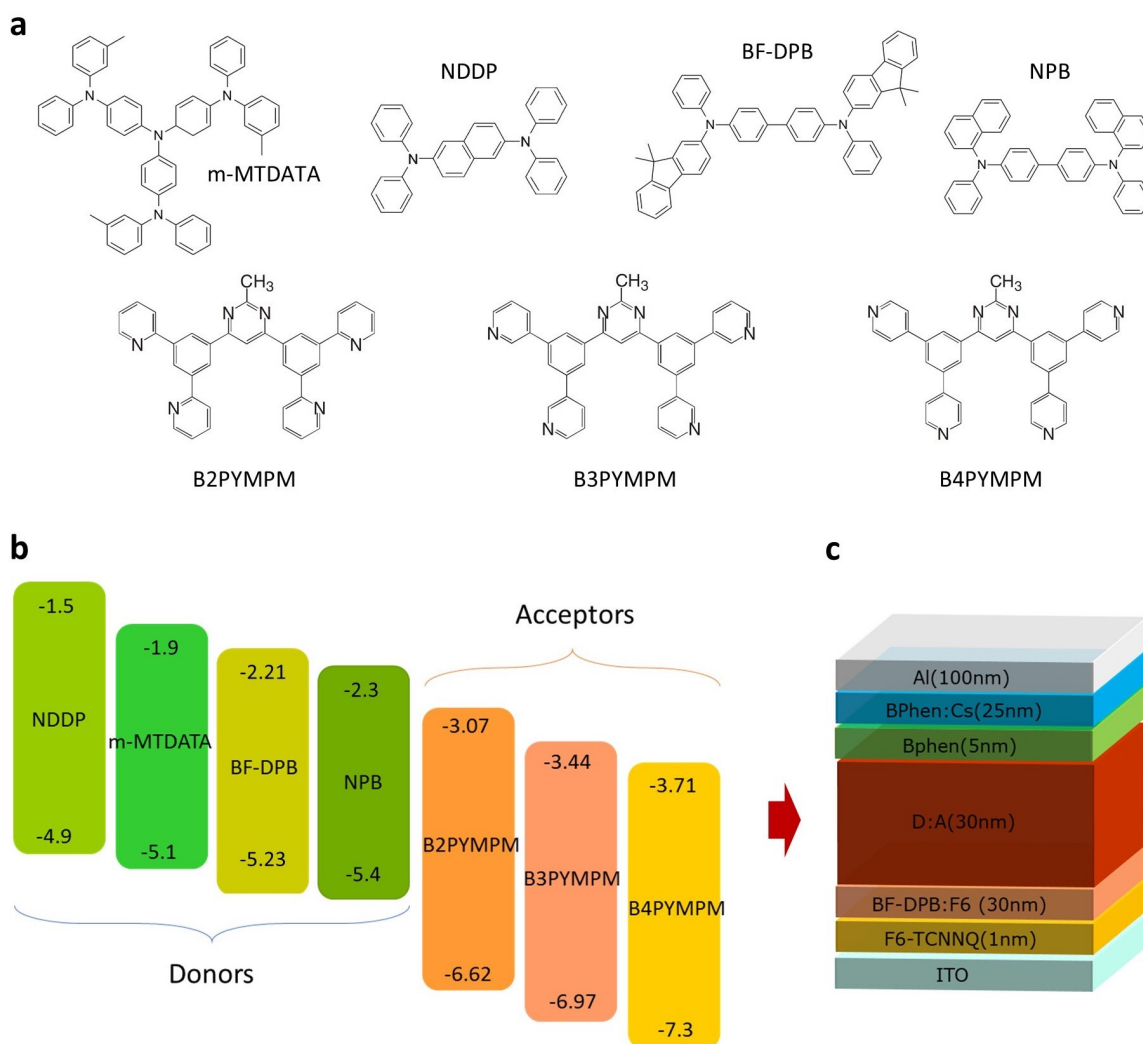
Summary

1. Materials and device structure

Figure S 1 a) Chemical structures of donor molecules, b) energy levels of the investigated molecules: NDDP,[1] m-MTDATA,[2] BF-DPB,[3,4] NPB,[3,5] B2PYMPM,[6] B3PYMPM,[6] B4PYMPM,[6] and c) device structure.

2. BHJ devices

Table S1. Photovoltaic performance of bulk heterojunction (BHJ) devices.

Donors	Acceptors	V_{OC} (V)	J_{SC} (mA cm^{-2})	FF (%)	PCE (%)
BF-DPB	B2PYMPM	2.21	0.22	19.1	0.09
NPB		2.29	0.20	23.1	0.10
m-MTDATA		2.00	0.20	30.0	0.12
NDDP		2.18	0.12	20.0	0.05
BF-DPB	B3PYMPM	2.16	0.57	35.0	0.43
NPB		2.18	0.36	35.8	0.28
m-MTDATA		1.86	0.17	42.2	0.13
NDDP		2.11	0.36	33.0	0.25
BF-DPB	B4PYMPM	2.02	0.55	72.0	0.80
NPB		2.00	0.46	76.3	0.70
m-MTDATA		1.67	0.22	69.2	0.26
NDDP		1.90	0.43	72.1	0.59
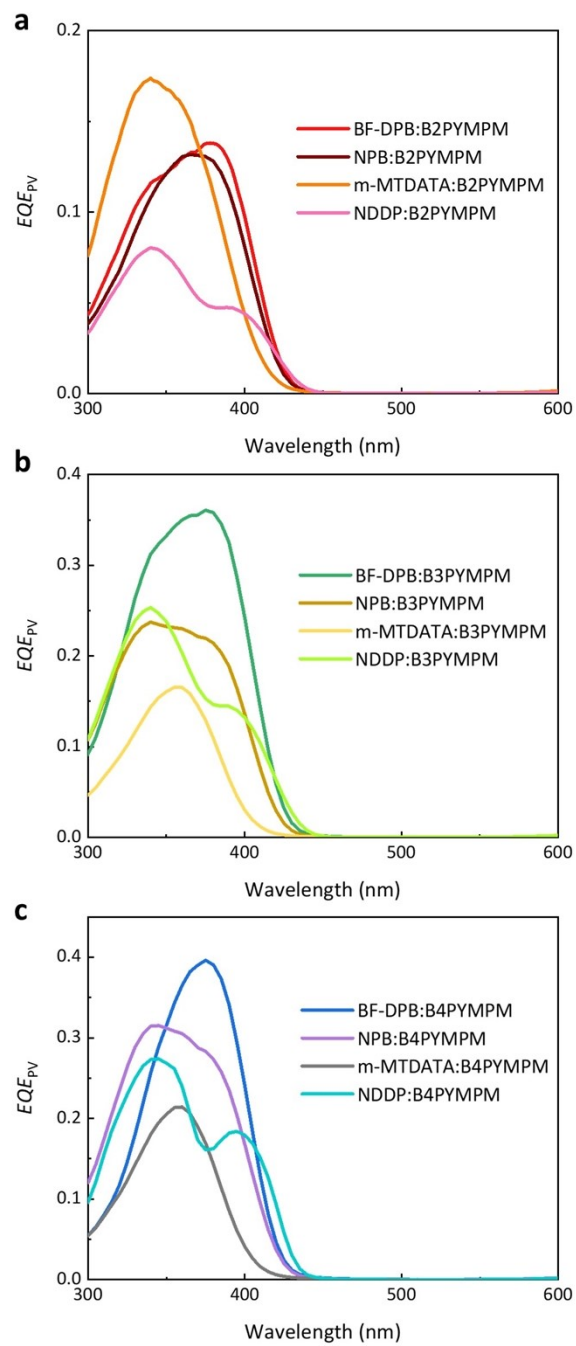
Figure S 2 Photovoltaic external quantum efficiency (EQE_{PV}) of BHJ devices.

a

b

V_{OC} = 1.97 V
J_{SC} = 0.56 mA cm-2
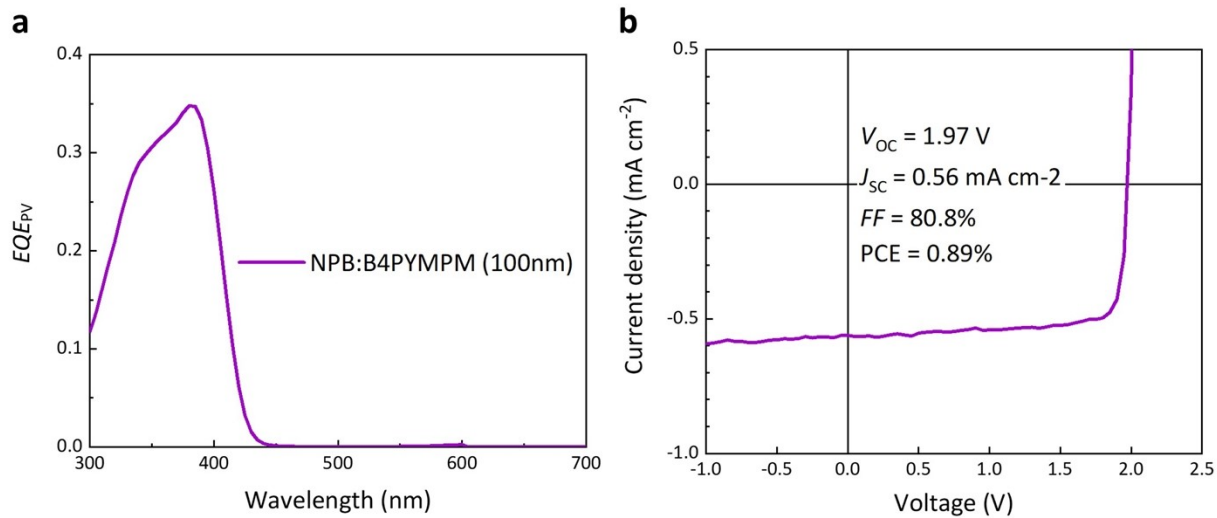*FF* = 80.8%
PCE = 0.89%

Figure S 3 Photovoltaic performance of NPB:B4PYMPM device with an active layer of 100 nm thick.

Table S2. Voltage and charge-transfer (CT) dissociation properties analysis of BF-DPB-based systems. E_{CT} is the energy of CT states, E_0 is the extrapolation of temperature-dependent suns-V_{OC} measurements to 0 K, and is a prompt for the energy of free charge carriers. The bound nature of CT is evaluated by the difference between E_0 and E_{CT}. Similarly, the difference between E_A and E_{CT} is evaluated, where E_A is the activation energy of electroluminescence. The EQE$_{EL}$ values are measured in the sensitive EL experiment, the injection current/voltage conditions are shown together with sensitive EL curves in Figure 2 in the main text and **Figure S 5**.

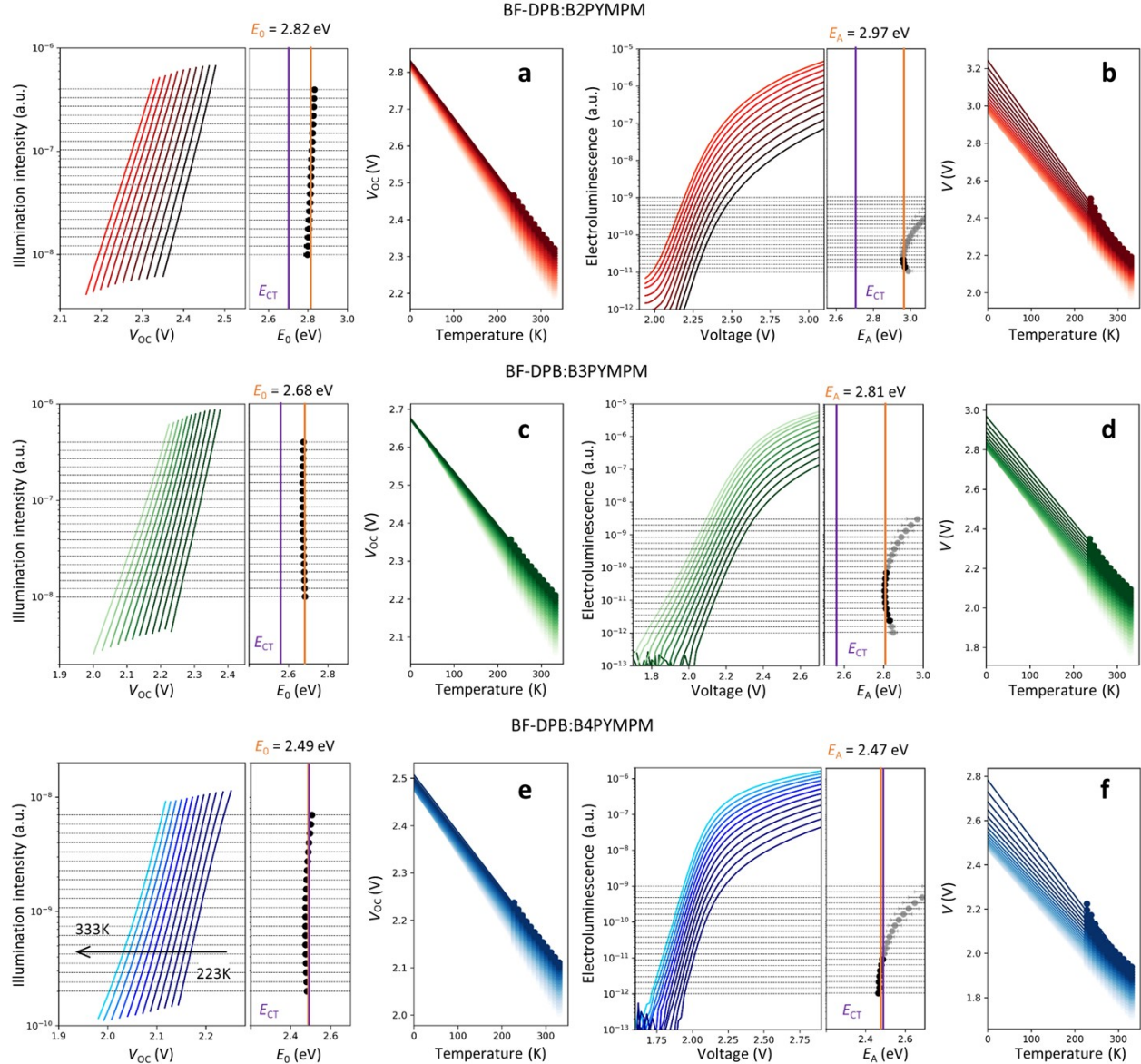| Donor	Acceptor	V_{OC} (V)	E_{CT} (eV)	E_0 (eV)	E_A (eV)	$E_0 - E_{CT}$ (eV)	$E_A - E_{CT}$ (eV)	EQE$_{EL}$ (%)
BF-DPB	B2PYMPM	2.21	2.71	2.82	2.97	0.11	0.26	0.06
BF-DPB	B3PYMPM	2.16	2.57	2.68	2.81	0.11	0.24	0.24
BF-DPB	B4PYMPM	2.02	2.49	2.49	2.47	0	-0.02	1.5

Figure S 4 Temperature-dependent suns-V_{OC} and EL measurements for BF-DPB-based systems. In all measurements, the temperature was varied between 223 K and 333 K in steps of 10 K, as indicated by the black arrow. Grey dashed lines indicate fixed light intensities or emitted photon counts at which the voltage is taken as a function of temperature. For suns-V_{OC} measurements, it provides a single energy value corresponding to eV_{OC} at 0 K for each intensity; while in EL measurements it produces an activation energy of electroluminescence (E_A) corresponding to eV at 0 K for each intensity. The corresponding fitted energies E_0 and E_A are shown in the middle panels as dots, with the error bars corresponding to fitting error. For fitted energies with fitting errors smaller than 15 meV, the average is taken and indicated by a vertical orange line. Fits of voltage changing with intensity and temperature are shown in right panels. For the grey activation energy points in the middle panels, the data deviates from the linear behavior, which is due to series resistances for EL measurements, but shunt resistance can influence both measurement types. The optically determined E_{CT} is plotted as a purple vertical line.
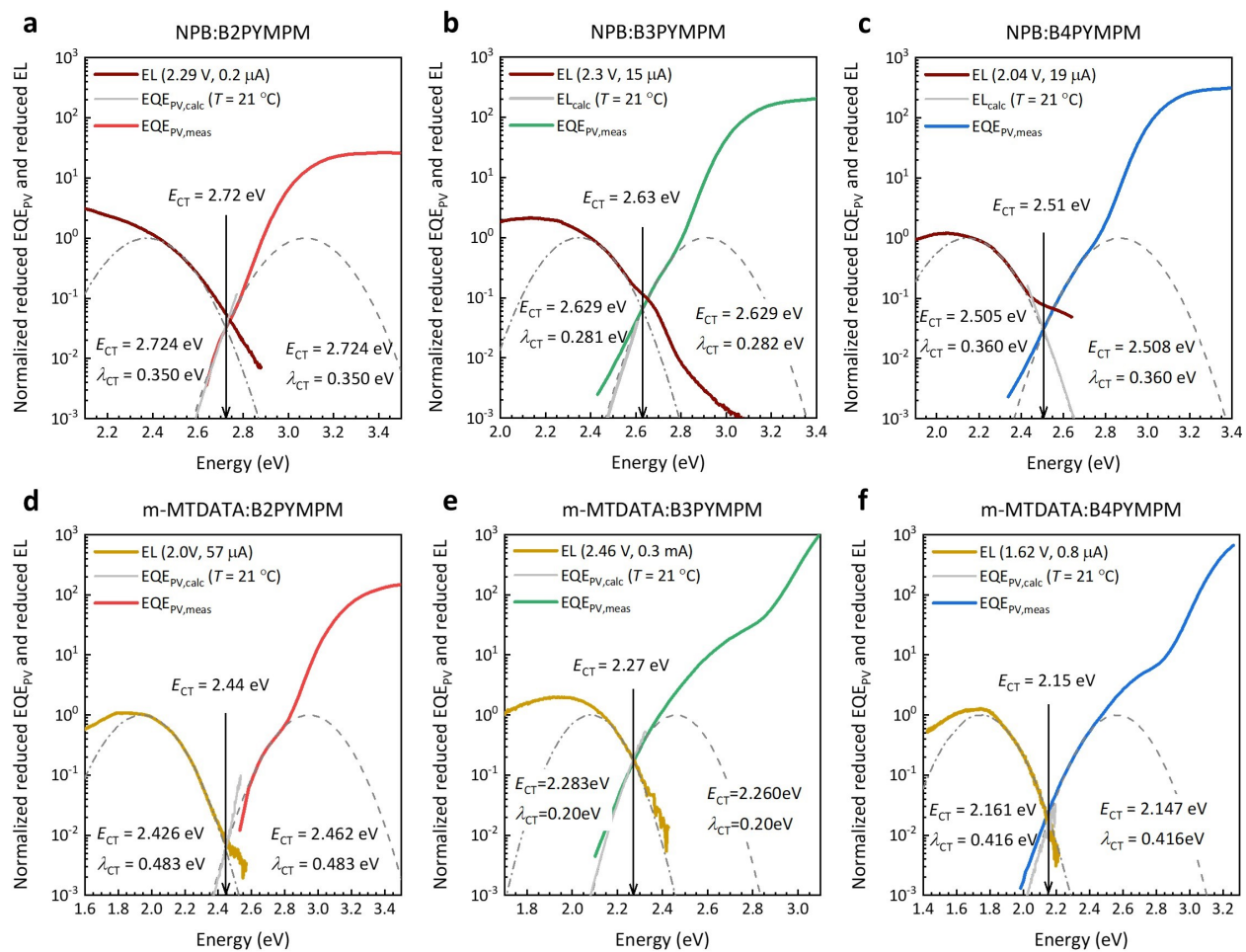
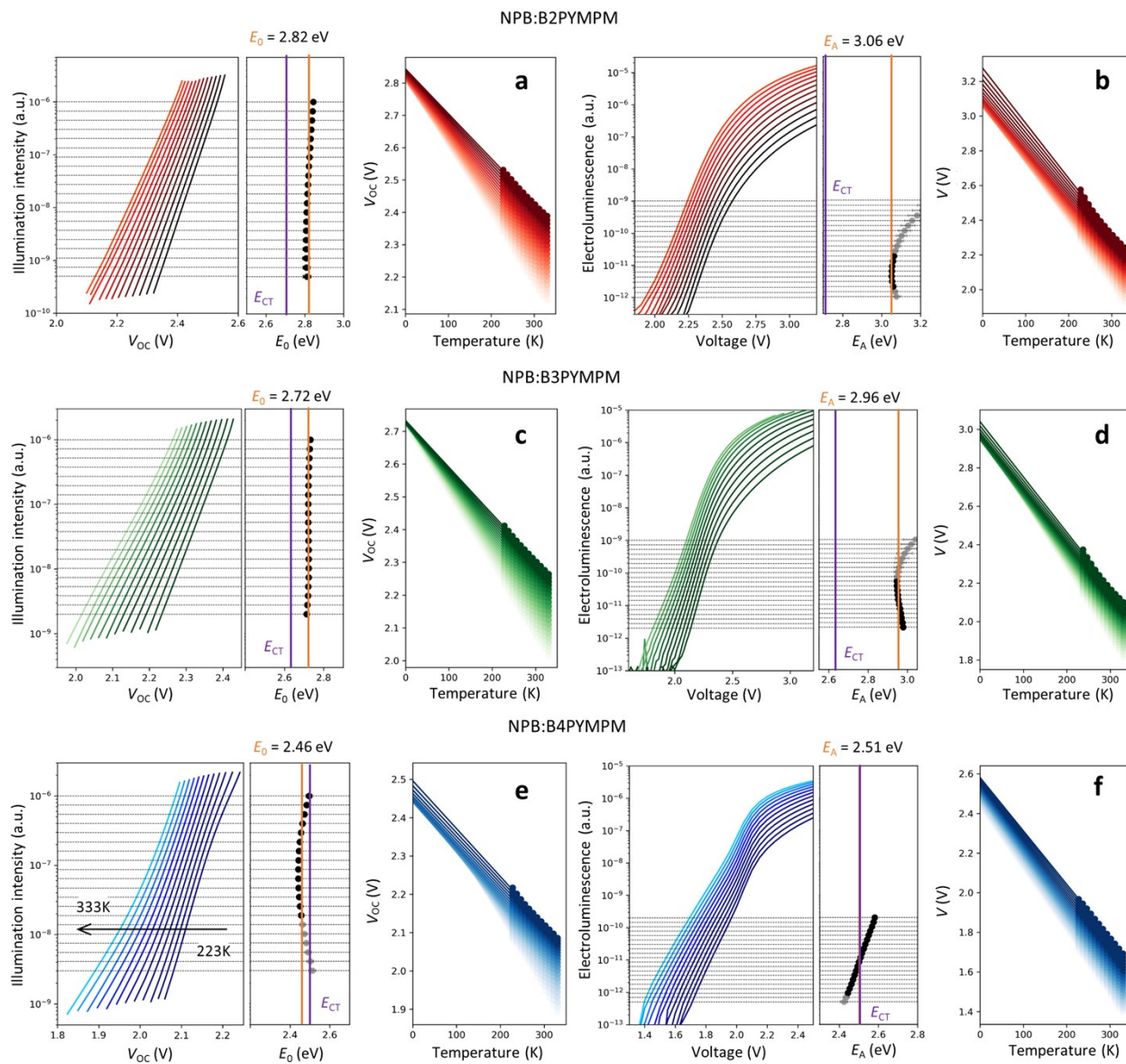**Figure S 5** Optical determination of the energy of CT states for BHJ NPB and m-MTDATA devices.

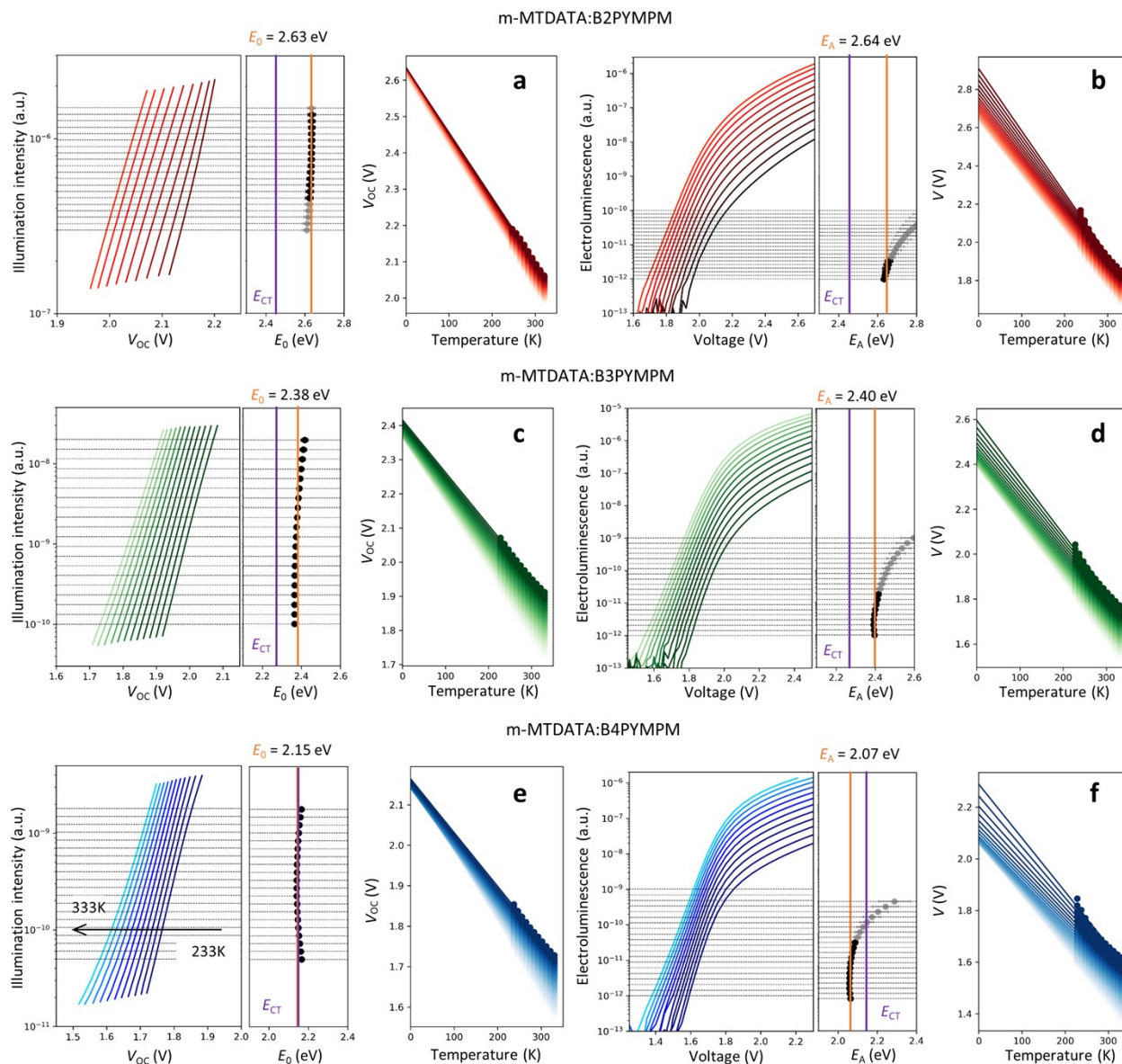**Figure S 6** Temperature-dependent suns-V_{OC} and EL measurements for NPB-based systems.

Figure S 7 Temperature-dependent suns-V_{OC} and EL measurements for m-MTDATA-based systems.

Table S3. Voltage and dissociation properties of CT for NPB- and m-MTADTA-based systems.

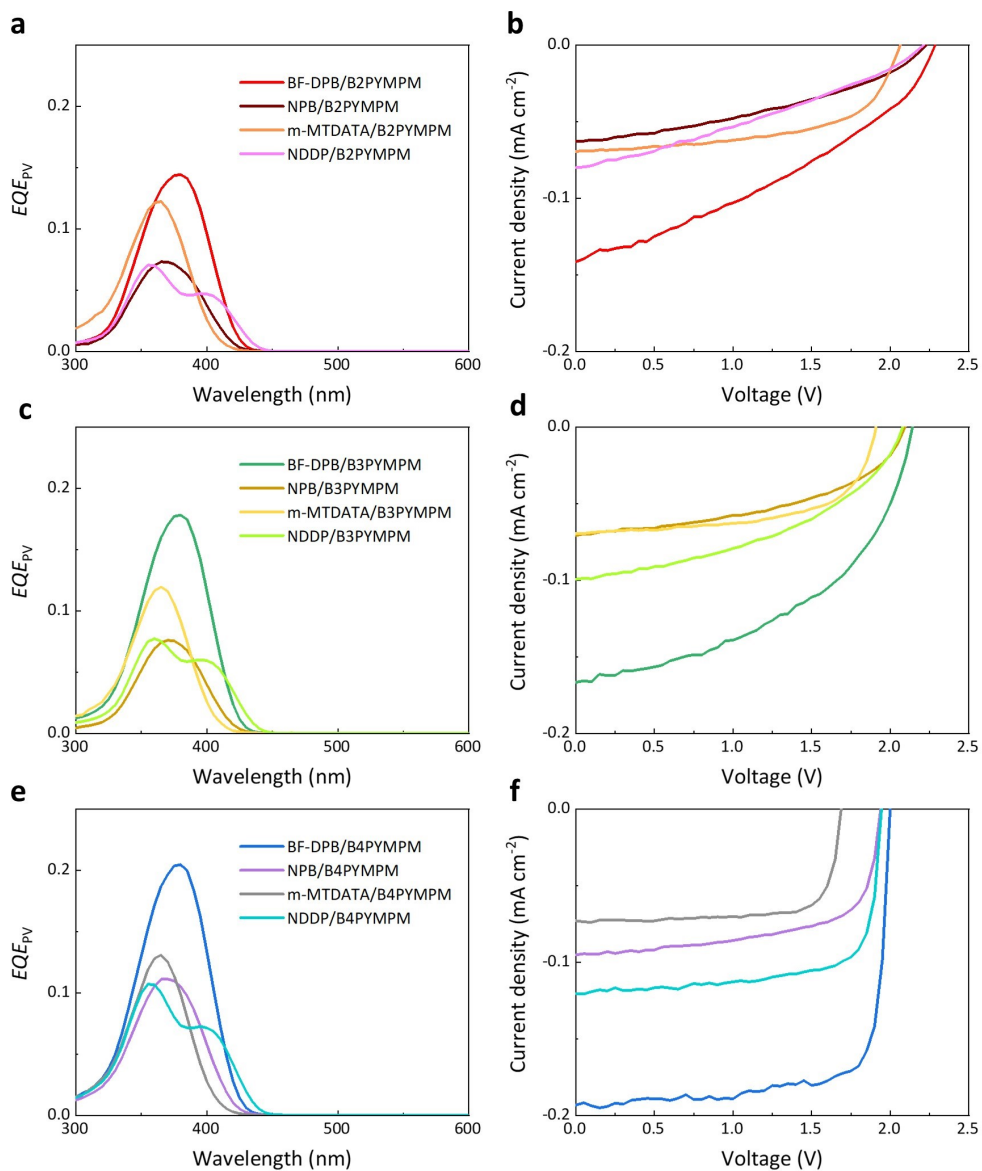| Donor	Acceptor	V_{OC} (V)	E_{CT} (eV)	E_0 (eV)	E_A (eV)	$E_0 - E_{CT}$ (eV)	$E_A - E_{CT}$ (eV)	EQE_{EL} (%)
NPB	B2PYMPM	2.29	2.72	2.82	3.06	0.10	0.34	0.2
	B3PYMPM	2.18	2.63	2.72	2.96	0.09	0.33	0.1
	B4PYMPM	2.00	2.51	2.46	2.51	-0.05	0	0.08
m-MTDATA	B2PYMPM	2.01	2.44	2.63	2.64	0.19	0.20	0.004
	B3PYMPM	1.86	2.27	2.38	2.40	0.11	0.13	0.28
	B4PYMPM	1.67	2.15	2.15	2.07	0	-0.08	0.07

3. PHJ devices

Figure S 8 Photovoltaic performance of planar heterojunction (PHJ) devices.

Table S4. Photovoltaic performance of PHJ devices.

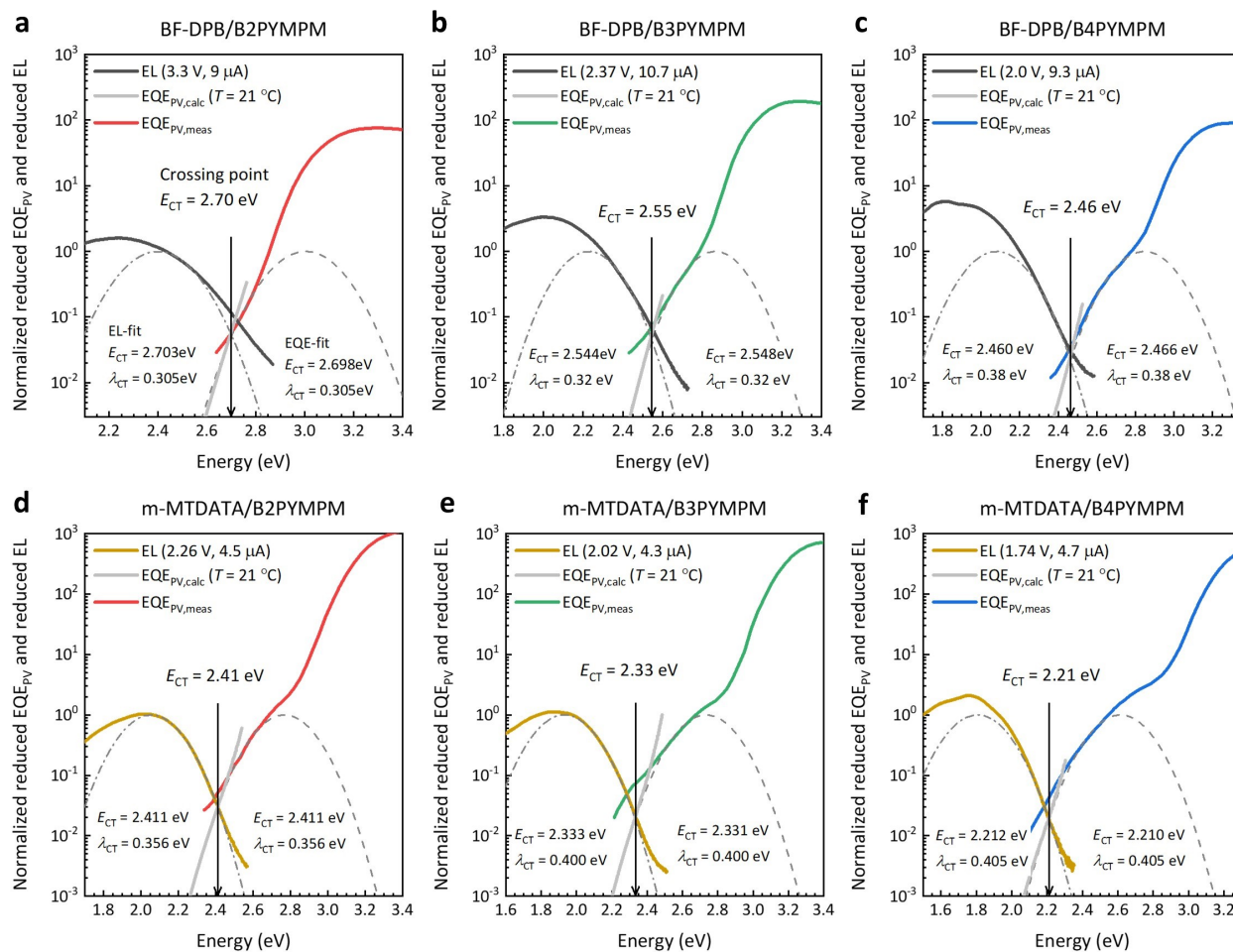| Donors	Acceptors	V_{OC} (V)	J_{SC} (mA cm^{-2})	FF (%)	PCE (%)
BF-DPB	B2PYMPM	2.29	0.13	36.6	0.11
NPB		2.23	0.06	38.6	0.05
m-MTDATA		2.06	0.07	57.9	0.08
NDDP		2.21	0.08	31.8	0.06
BF-DPB	B3PYMPM	2.14	0.16	47.4	0.16
NPB		2.10	0.07	47.0	0.07
m-MTDATA		1.91	0.07	60.7	0.08
NDDP		2.08	0.09	43.7	0.09
BF-DPB	B4PYMPM	2.00	0.18	78.1	0.28
NPB		1.94	0.09	64.1	0.12
m-MTDATA		1.69	0.07	76.6	0.09
NDDP		1.94	0.12	72.2	0.17

Figure S 9 Optical determination of the energy of CT states for PHJ devices.
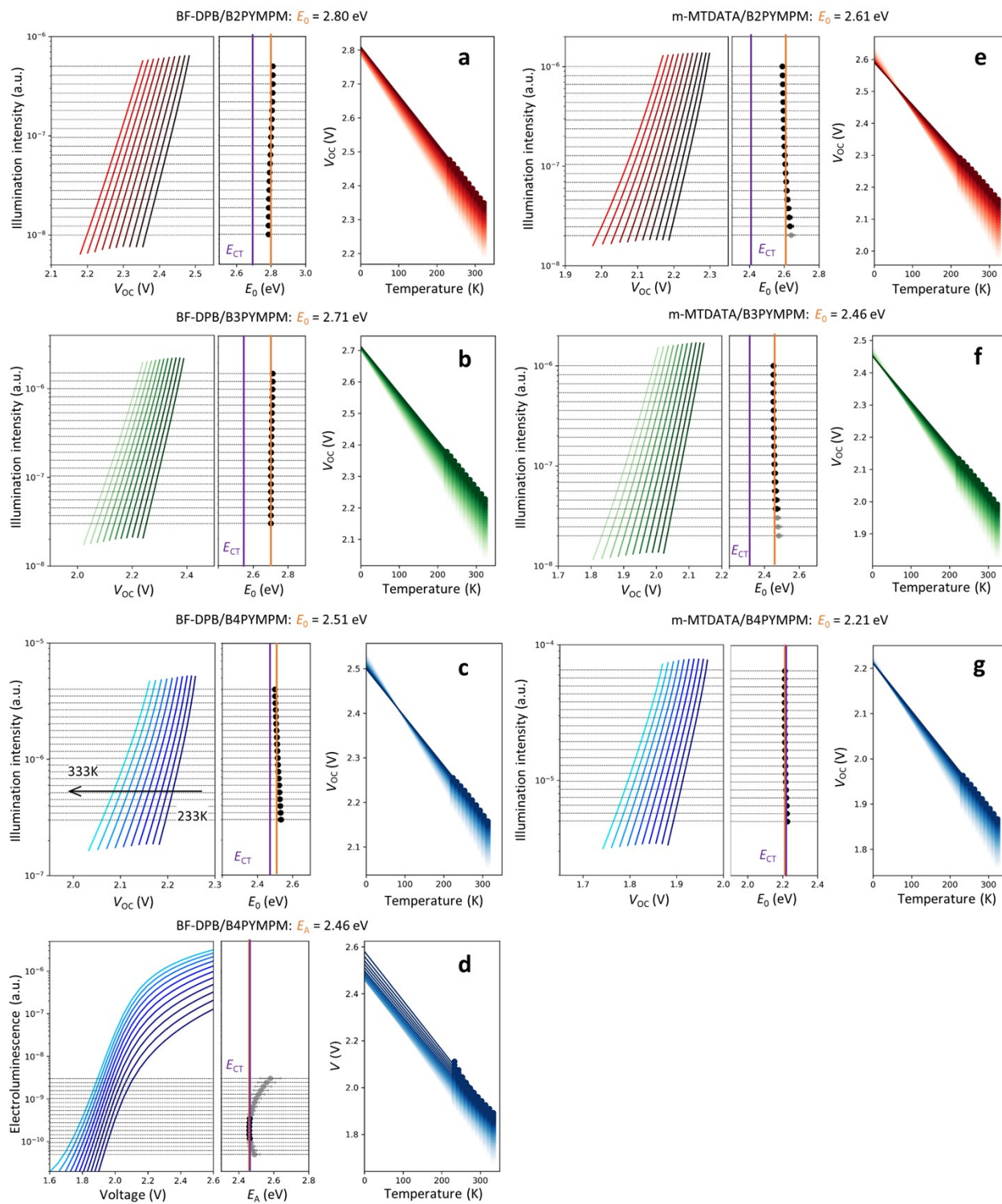
Figure S 10 Temperature-dependent suns-V_{OC} and EL measurements for PHJ devices.

Table S5. Voltage and dissociation properties of CT analysis of PHJ devices.

Donor	Acceptor	V_{OC} (V)	E_{CT} (eV)	E_0 (eV)	E_A (eV)	$E_0 - E_{CT}$ (eV)	EQE_{EL} (%)
BF-DPB	B2PYMPM	2.29	2.70	2.80	-	0.10	0.14
	B3PYMPM	2.14	2.55	2.71	-	0.16	0.031
	B4PYMPM	2.00	2.46	2.51	2.46	0.05	0.037
m-MTDATA	B2PYMPM	2.06	2.41	2.61	-	0.20	0.196
	B3PYMPM	1.91	2.33	2.46	-	0.13	0.04
	B4PYMPM	1.69	2.21	2.21	-	0	0.0032

4. GIWAXS data

Here we report 2D GIWAXS patterns of B2PYMPM, B3PYMPM and B4PYMPM pristine films on silicon substrates (**Figure S 11**a-c). The corresponding population orientation analysis are shown in **Figure S 11**d-f (where an angle of 90 degrees means completely lying-down alignment and an angle of 0 degrees represents a standing-up arrangement with respect to the substrate). In the pattern of neat B4PYMPM film, the scattering vector q of 1.73 Å-1 on the Qz axis is attributed to the π-π stacking diffraction, suggesting a typical face-on molecular orientation. This coincides with the population analysis in which 44.8% of B4PYMPM molecules have an orientation angle in the range of 60-80 degrees, surpassing those of B2PYMPM (12.2%) and B3PYMPM (30.8%). In fact, most of B2PYMPM molecules are isotropically oriented (62.6%) as shown in **Figure S 11**d and Table S6. Compared to neat acceptor films, blends of the acceptors with BF-DPB show a relatively higher isotropic percentage that, together with the significant increase in the peak width, suggests more amorphous molecular orientations in the blend films, caused by the introduction of the amorphous donor material BF-DPB (**Figure S 12** and Table S7). However, B4PYMPM-based blend films still show the highest face-on ratio among blend films.
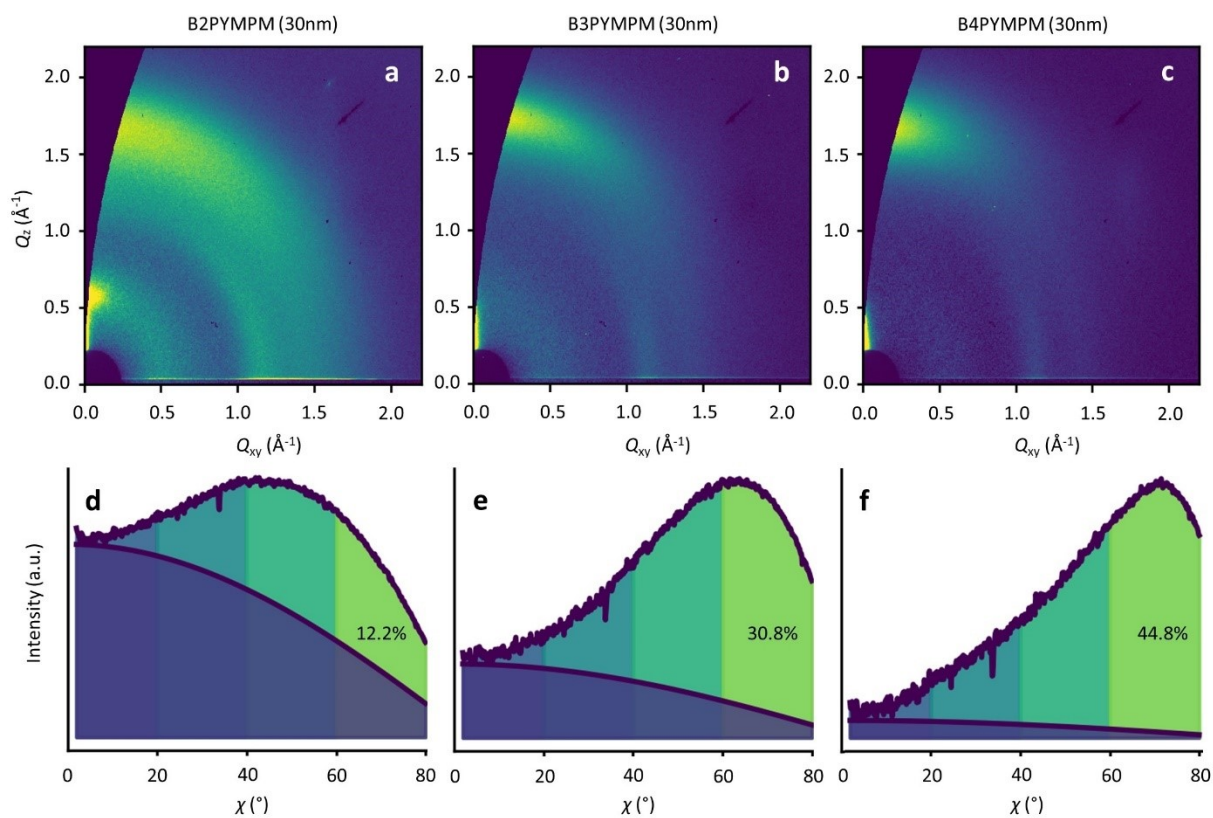
Figure S 11 Morphology characterization. a-c) GIWAXS data of 30 nm thick neat B2PYMPM, B3PYMPM, and B4PYMPM deposited on silicon substrate, respectively. d-f) Corresponding population orientation analysis. The blue area visible at all angles denotes the intensity originating from isotropic orientated molecules. Angle χ equal to 0 degree indicates a fully edge-on molecular alignment, while a χ value of 90 degrees represents a completely face-on orientation for the π-π stacking diffraction.

Table S6. Analysis of orientation population in pristine acceptor films deposited on silicon substrate.

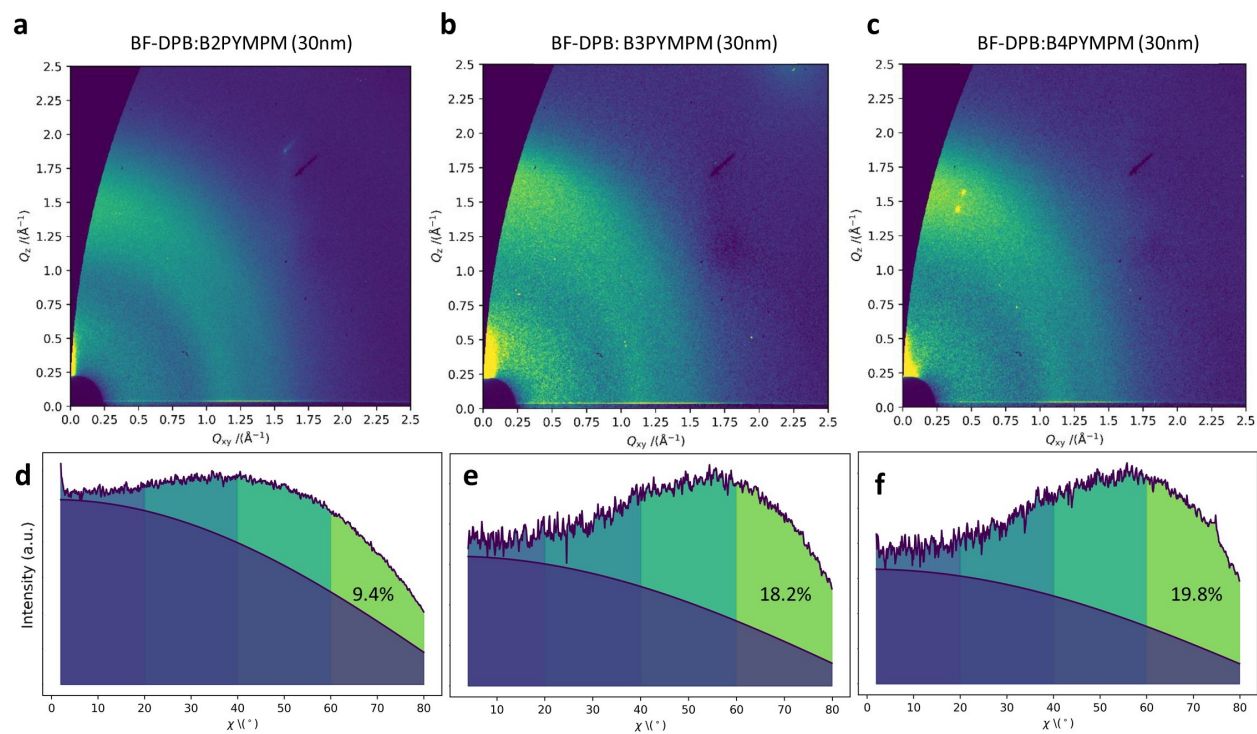| Orientation	Si/B4PYMPM	Si/B3PYMPM	Si/B2PYMPM
isotropic	9.2 %	30.4 %	62.6 %
0°–20°	3.3 %	2.2 %	1.8 %
20°–40°	13.4 %	10.5 %	8.6 %
40°–60°	29.4 %	26.0 %	14.8 %
60°–80°	44.8 %	30.8 %	12.2 %

Figure S 12 GIWAXS measurements for BF-DPB:Acceptor mixed films deposited on silicon substrates and the corresponding population orientation analysis. The strong increase in the signal originating from isotropically orientated molecules is attributed to the introduction of the amorphous donor material BF-DPB.

Table S7. Analysis of orientation population in BF-DPB:Acceptor mixed films on silicon substrate.

Orientation	Si/BF-DPB:B4PYMPM	Si/BF-DPB:B3PYMPM	Si/BF-DPB:B2PYMPM
isotropic	47.4 %	52.2 %	71.5 %
0°–20°	3.3 %	2.7 %	1.7 %
20°–40°	10.0 %	8.6 %	6.4 %
40°–60°	19.5 %	18.3 %	10.9 %
60°–80°	19.8 %	18.2 %	9.4 %

5. Charge generation, recombination and relation to temperature dependence of the open-circuit voltage

Below, we will derive equations for the open-circuit voltage V_{oc} in two cases.[7]

1. Charge generation happens through thermalized charge transfer (CT) states, the same states are reformed upon charge recombination. All charges come from these CT states.

2. Charge generation happens through a separate channel, but charge recombination populates thermalized CT states, from which free charge formation can occur again through CT dissociation. For this second case we will derive the results for:

   i.   Bound CT states $(k_d \ll k_f)$

   ii. Unbound CT states $(k_d \gg k_f)$

We will show that in case 1 and 2.ii, the extrapolated value of V_{oc} to 0 K, which is E_0 in the main text, equals E_{CT}; while in case 2.i, E_0 will equal the energy of an unbound pair of free charge carriers E_{FCC}.
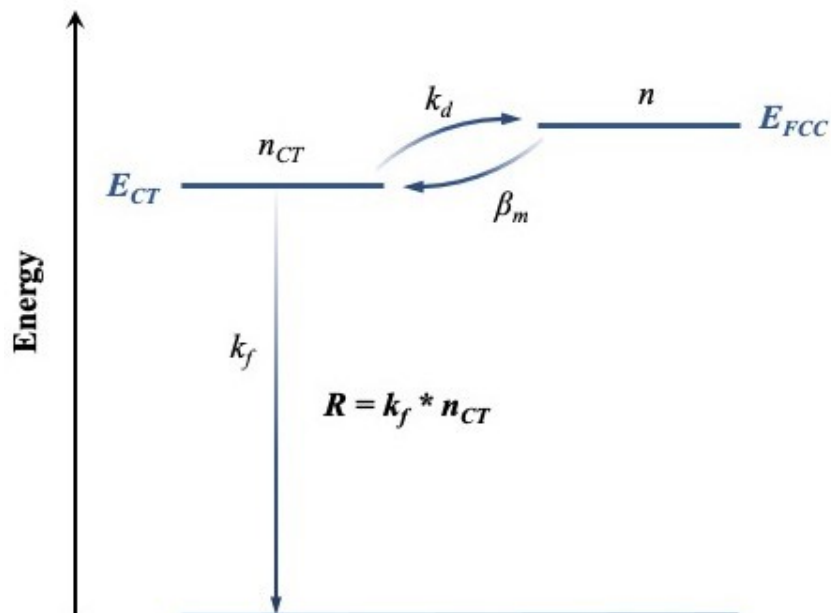

Figure S 13 Simple three states model for the CT state dissociation properties.

Consider the simplified energy diagram, showing energies and rates of CT states and free charge carriers (FCC).

We assume same electrons and holes densities, as well as same site densities for electrons and holes. In darkness and no voltage applied, the density of occupied CT states is:

$$n_{CT}^0 = N_{CT} exp\left(-\frac{E_{CT}}{k_B T}\right) \qquad 5.1$$

where N_{CT} is the density of CT states, E_{CT} the energy difference between the CT state and the ground state, k_B the Boltzmann constant, and T the temperature of the blend. Similarly, the density of occupied FCC states n_i^2, in darkness and no voltage applied, is:

$$n_i^2 = N_{FCC}^2 exp\left(\frac{-E_{FCC}}{k_B T}\right) \qquad 5.2$$

N_{FCC} represents the density of states for electrons (holes), E_{FCC} the energy of FCC states. Without influence from light illumination and/or applied bias, charge generation through CT dissociation and CT reformation through free charges recombination are in equilibrium:

$$k_d n_{CT}^0 = \beta_m n_i^2 \qquad 5.3$$

$$k_d N_{CT} exp\left(-\frac{E_{CT}}{k_B T}\right) = \beta_m N_{FCC}^2 exp\left(-\frac{E_{FCC}}{k_B T}\right) \qquad 5.4$$

$$k_d = \beta_m N_{FCC}^2 N_{CT}^{-1} exp\left(-\frac{E_{FCC} - E_{CT}}{k_B T}\right) \qquad 5.5$$

k_d denotes the rate constant for the dissociation of CT states, β_m is the coefficient for encounter of FCC.

Under light illumination or with applied voltage, the density of occupied FCC states increases exponentially with the bulk Fermi-level splitting (QFLS):

$$n^2 = n_i^2 exp\left(\frac{QFLS}{k_BT}\right) = N_{FCC}^2 exp\left(\frac{QFLS - E_{FCC}}{k_BT}\right)$$ 5.6

In absence of surface recombination, qV_{OC} upon illumination is equal to the QFLS. Therefore:

$$qV_{OC} = QFLS = E_{FCC} + k_BTln\left(\frac{n^2}{N_{FCC}^2}\right)$$ 5.7

This is true irrespective of how charges are generated and how they recombine. Below, we consider two limiting cases: case 1 assumes that the CT states involved in the charge generation process are the same as the ones involved in the charge recombination process. In contrast, case 2 assumes that charge generation bypasses the lowest energy CT state and that only when free carriers recombine, a low energy CT state is formed.
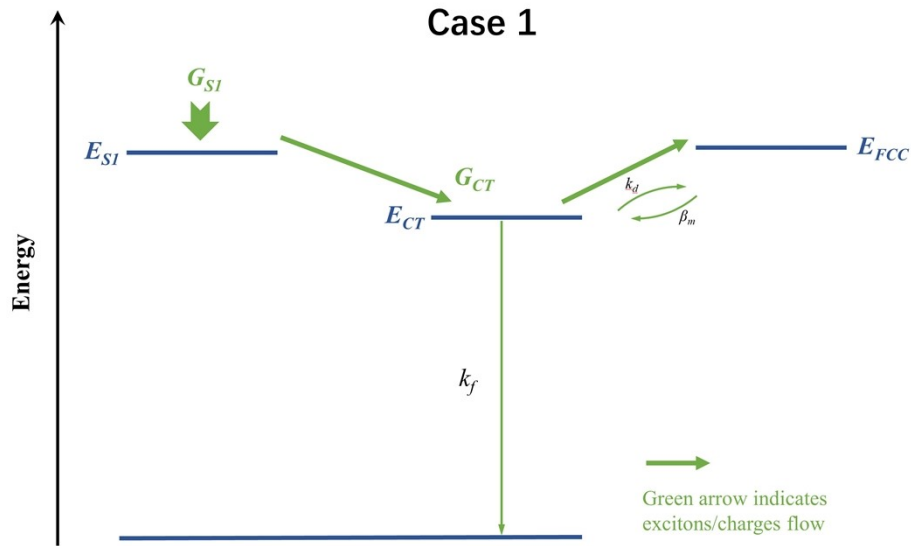
5.1. Case 1:

Figure S 14 Schematic representation for Case 1. G_{SI} indicates the generation rate of singlet state and G_{CT} is the generation rate of CT state. k_d presents the dissociation rate of CT excitons to free charge carriers and β_m the recombination rate of free charge carriers to CT states. k_f is the decay rate of CT excitons to ground state.

Considering a cell working in a steady state, all populations are constant in time. We now assume that charges are only generated via the same CT state through which free charges recombine. Also, the CT generation rate is equal to the exciton generation rate ($G_{CT} = G_{S1} = G$, assuming all excitons reach the interface and dissociate). Finally, because we are at V_{OC} conditions, no carriers are extracted. Therefore, all carriers must recombine again, which we assume to proceed entirely through the repopulation of the same CT states through which free charges have been generated (we neglect here surface and SRH recombination). Then:

$$\frac{dn_{CT}}{dt} = 0 = G - k_f n_{CT} + \beta_m n^2 - k_d n_{CT} \qquad 5.8$$

$$\frac{dn}{dt} = + k_d n_{CT} - \beta_m n^2 = 0 \qquad 5.9$$

k_f denotes the rate constant for the decay of CT states. Then:

$$n_{CT} = \frac{G}{k_f} \qquad 5.10$$

$$n^2 = \frac{k_d}{\beta_m} n_{CT} \qquad 5.11$$

irrespective of the generation-recombination balance of charges. By using equation 5.5:

$$n^2 = \frac{k_d}{\beta_m} n_{CT} = \frac{k_d \, G}{\beta_m k_f} = N_{FCC}^2 N_{CT}^{-1} \frac{G}{k_f} \exp\left(-\frac{E_{FCC} - E_{CT}}{k_B T}\right) \qquad 5.12$$

Then, at V_{OC} it follows that:

$$qV_{OC} = E_{FCC} + k_B T ln\left(\frac{n^2}{N_{FCC}^2}\right) = E_{FCC} + k_B T ln\left(N_{CT}^{-1} \frac{G}{k_f} \exp\left(-\frac{E_{FCC} - E_{CT}}{k_B T}\right)\right) =$$

$$= E_{CT} + k_B T ln\left(N_{CT}^{-1} \frac{G}{k_f}\right) \qquad 5.13$$

Equation 5.13 indicates that under illumination the V_{OC} is entirely determined by the CT properties. This is irrespective of the CT dissociation barrier and the dissociation rate.
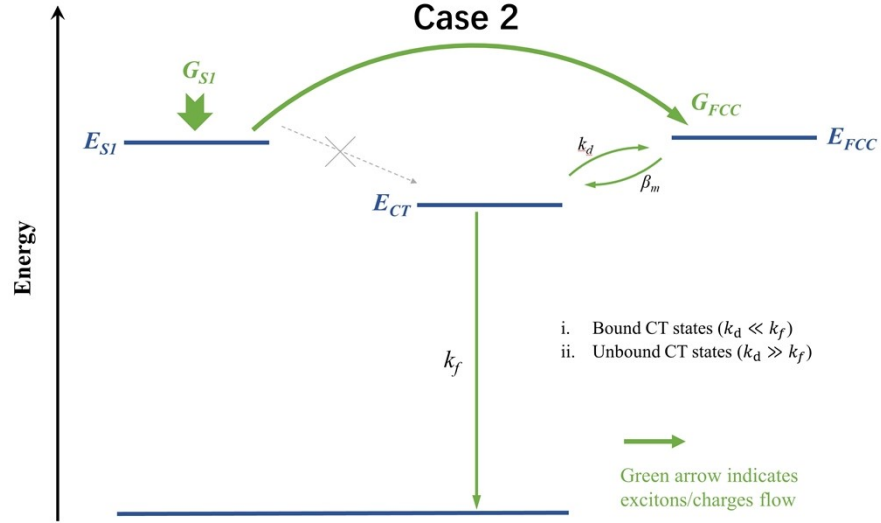
5.2. Case 2:

Figure S 15 Schematic representation for Case 2. G_{FCC} indicates the generation rate of FCC directly from S1 state.

In this case 2, exciton dissociation generates free charges via a mechanism not involving the lowest energy CT state. Then the free charges generation rate is $G_{FCC} = G_{S1} = G$. In steady state:

$$\frac{dn_{CT}}{dt} = -k_d n_{CT} - k_f n_{CT} + \beta_m n^2 = 0 \qquad 5.\,14$$

$$\frac{dn}{dt} = +G + k_d n_{CT} - \beta_m n^2 = 0 \qquad 5.\,15$$

Then:

$$n_{CT} = \frac{\beta_m}{k_d + k_f} n^2 \qquad 5.\,16$$

$$G = -k_d \frac{\beta_m}{k_d + k_f} n^2 + \beta_m n^2 = \beta_m \left(-\frac{k_d}{k_d + k_f} + 1 \right) n^2 =$$

$$= \beta_m\left(\frac{k_f}{k_d + k_f}\right)n^2 = k_2 n^2 \qquad 5.17$$

Here, $k_2 = \beta_m\left(\frac{k_f}{k_d + k_f}\right)$ is the charge recombination coefficient that takes into account resplitting of CT states. It follows that for V_{OC}:

$$qV_{OC} = E_{FCC} + k_B T ln\left(\frac{n^2}{N_{FCC}^2}\right) = E_{FCC} + k_B T ln\left(\frac{G}{k_2 N_{FCC}^2}\right) \qquad 5.18$$

Now let us consider two extreme cases.

In case (i), CT recombination is faster than dissociation ($k_d \ll k_f$, bound CT states), $k_2 = \beta_m\left(\frac{k_f}{k_d + k_f}\right) = \beta_m$, which is proportional to the mobilities. Assuming that $\beta_m = \beta_m^0 exp\left(-\frac{E_{A,\mu}}{k_B T}\right)$ and $G = G^0 exp\left(-\frac{E_{A,G}}{k_B T}\right)$, this results in:

$$qV_{OC} = E_{FCC} - E_{A,G} + E_{A,\mu} + k_B T ln\left(\frac{G^0}{\beta_m^0 N_{FCC}^2}\right) \qquad 5.19$$

Which also contains the activation energies for charge generation and recombination (taking into account that also the charge generation may be temperature dependent).

In case (ii), CT dissociation is very efficient ($k_d \gg k_f$, unbound CT states). Then, using again equation 5.5:

$$k_2 = \beta_m\left(\frac{k_f}{k_d + k_f}\right) = k_f\frac{\beta_m}{k_d} = k_f N_{FCC}^{-2} N_{CT} exp\left(+\frac{E_{FCC} - E_{CT}}{k_B T}\right) \qquad 5.20$$

It follows that:

$$qV_{OC} = E_{FCC} + k_B T ln\left(\frac{G}{k_2 N_{FCC}^2}\right) = E_{FCC} + k_B T ln\left(\frac{G}{k_f N_{CT}} exp\left(-\frac{E_{FCC} + E_{CT}}{k_B T}\right)\right) =$$
$$= E_{CT} + k_B T ln\left(\frac{G}{k_f N_{CT}}\right) \qquad 5.21$$

Which is the same expression as for case 1.

6. Computational protocol details

6.1. Force field molecular dynamics simulations

We opted for a customized force field based on the General AMBER Force Field (GAFF) for organic molecules (version 1.4, March 2010).[8] The parameters for the most relevant degrees of freedom were determined in order to reproduce the DFT energy profiles. In particular, the FF parameters were obtained by means of an *in-house* Python code, specifically designed to iteratively fit the potential energy surfaces of bonds, angles and soft dihedral angles responsible for inter-rings reciprocal motions (see **Figure S 16**). In addition, during the fitting procedure, small variations of some Lennard-Jones potential coefficients were allowed. Atomic charges were obtained by fitting the electrostatic potential (ESP charges) calculated at the optimized B3LYP/6-31G(d) geometry; then, ESP charges were properly symmetrized in order to satisfy the symmetry properties of the molecules (see **Figure S 17**). All DFT calculations were performed using the GAUSSIAN16 suite (except where explicitly stated).[9]

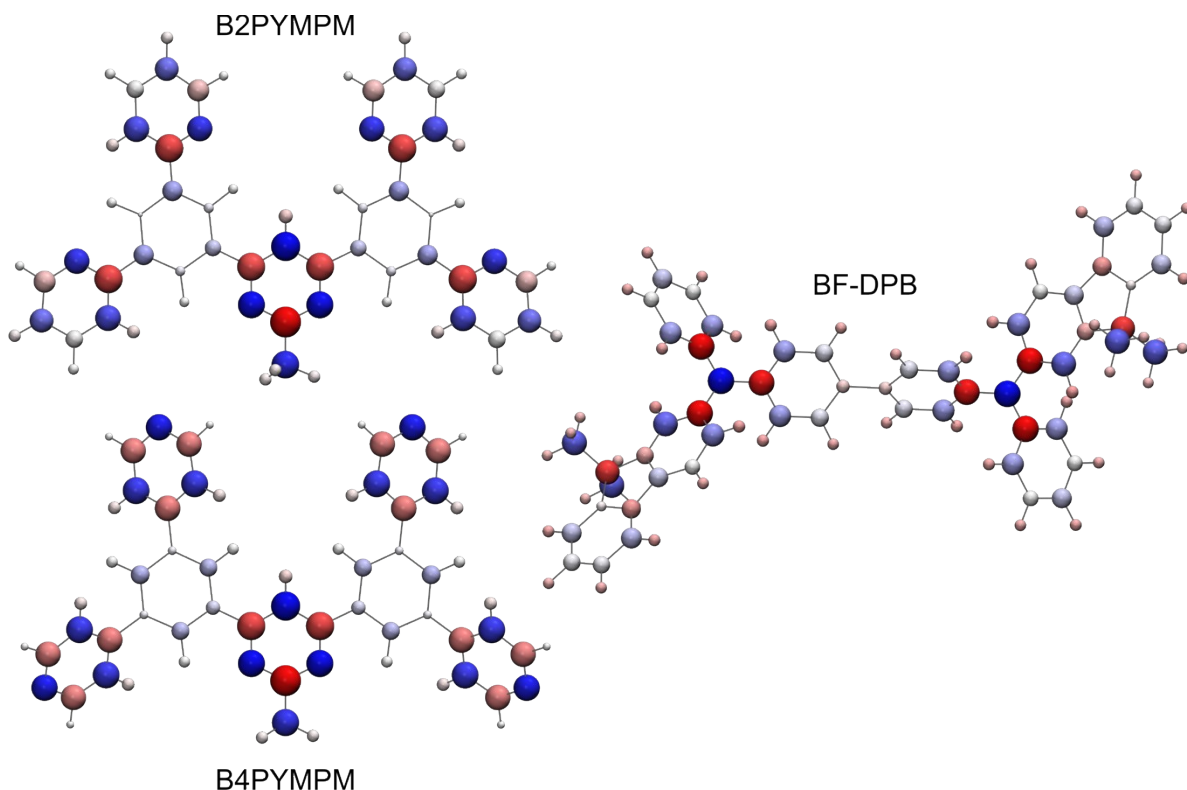**Figure S 16** Representation of the three molecular structures, with blue shaded highlighting of the force field (FF) re-parametrized degrees of freedom involving bonds, angles and dihedral angles. Atom types defined in the FF are also reported.

Figure S 17 Representation of the symmetrized ESP charges of BF-DPB, B2PYMPM and B4PYMPM. Spheres volume and color (red for positive and blue for negative charges) are proportional to the atomic partial charge.

Two donor:acceptor (D:A) planar heterojunction (PHJ) samples were built by means of molecular dynamics (MD) simulations using the re-parametrized FF. The first sample consisted in a BF-DPB:B2PYMPM junction between amorphous phases, while the second one in an amorphous BF-DPB: crystalline B4PYMPM interface. In particular, the acceptor phases (either the amorphous B2PYMPM or the crystalline B4PYMPM) were initially built starting from the crystallographic unit cell of a similar molecule (B4PyPTZ) available in the Cambridge Crystallographic Data Center, no. CCDC-1030701,[10] and replacing the coordinates of the atoms of 16 B4PyPTZ molecules in the unit cell with those of B2PYMPM or B4PYMPM. All MD simulations were performed with the NAMD software,[11] using a timestep of 1 fs, 3D periodic boundary conditions (PBC) and the particle mesh Ewald summation for electrostatic interactions, a cutoff of 12 Å for Lennard-Jones interactions, the velocity rescaling thermostat and the Berendsen barostat (except where explicitly stated). Specifically:

- Simulation of the B2PYMPM amorphous phase: a large cubic box of side 150 Å was filled with 720 B2PYMPM molecules, yielding an initial, low mass density of 0.200 g/cm^3. Then, a series of MD runs were subsequently performed: a) an NVT run for 1 ns at 2000 K to randomize

molecular orientations; b) an NPT run for 2.5 ns at 1000 K and 1000 atm; c) an NPT run for 2.5 ns at 500 K and 100 atm; d) an NPT run for 2.5 ns at 500 K and 10 atm; e) an NPT run for 2.5 ns at 500 K and 1 atm; f) an NPT run for 2.5 ns at 298 K and 1 atm. The final parameters of the orthorhombic cell were a = 82.53 Å, b = 83.94 Å and c = 81.79 Å with a final mass density of 1.171 g/cm^3.

- Simulation of the B4PYMPM crystal phase: a crystalline 3×5×3 supercell with 720 B4PYMPM molecules was built, and an NPT MD run of 5 ns at 298 K and 1 atm was performed. At the end of the simulation, the structural parameters and the mass density reached equilibration and the monoclinic structure of the parental crystal was preserved. The final cell parameters were a = 71.11 Å, b = 91.66 Å and c = 82.86 Å with a final mass density of 1.238 g/cm^3.

- Simulation of the BF-DPB amorphous phase: 720 BF-DPB molecules were placed in an orthorhombic box with the same a and b length of either the amorphous B2PYMPM supercell or the crystalline B4PYMPM, while c was set equal to 200 Å. Both the BF-DPB donor samples were subjected to an NVT MD run of 1 ns and at 2000 K in order to randomize molecular positions.

- Assembly of the two heterojunctions: BF-DPB samples were opportunely translated and placed either on top of the B2PYMPM or B4PYMPM samples along the c direction. The atomic positions of the resulting D:A bilayers were then minimized by using a steepest-descendent algorithm (5000 steps).

- Equilibration of the two heterojunctions: at last, an NPT run of 70 ns at 298 K and 1 atm was performed on the two bilayers, where the Langevin piston was applied in order to compress the simulation box only along the long c axis, while keeping constant the a and b cell parameters.

At the end of the MD simulations, the amorphous BF-DPB: B2PYMPM sample yielded the following parameters: a = 82.53 Å, b = 83.94 Å and c = 196.39 Å, $\alpha = \beta = \gamma = 90°$, while the amorphous BF-DPB : crystalline B4PYMPM sample yielded the following parameters: a = 71.11 Å, b = 91.66 Å and c = 208.67 Å, $\alpha = \gamma = 90°$ and $\beta = 98.3°$.

The density (ρ) of BF-DPB and of the two acceptors as a function of the z coordinate (the c axis is perpendicular to the interface) is plotted in **Figure S 18**, showing the different positional order between the acceptor phases in the two samples: while the density of B2PYMPM is rather uniform, the one of B4PYMPM shows a series of periodic peaks corresponding to the π-stacking distance between face-on molecules organized in columns normal to the interface (~3.5 Å). Concerning the orientational order, the order parameter $\langle P_2 \rangle = \frac{3}{2}\langle(\hat{u} \cdot \hat{z})^2\rangle - \frac{1}{2}$ was calculated using as a molecular axis $\hat{u}$ with the lowest inertia moment, *i.e.*, the one normal to the π-stacking direction, and the

direction $\hat{z}$ normal to the interfacial plane as reference alignment axis.[12] As expected from the adopted simulation protocol, B2PYMPM and BF-DPB did not show any strong preferential alignment ($\langle P_2 \rangle_{B2PYMPM} = -0.013$, $\langle P_2 \rangle_{BF-DPB} = -0.104$ and $= -0.114$ in the B2PYMPM and B4PYMPM samples, respectively), while B4PYMPM exhibits a very high orientational order ($\langle P_2 \rangle_{B4PYMPM} = -0.498$).
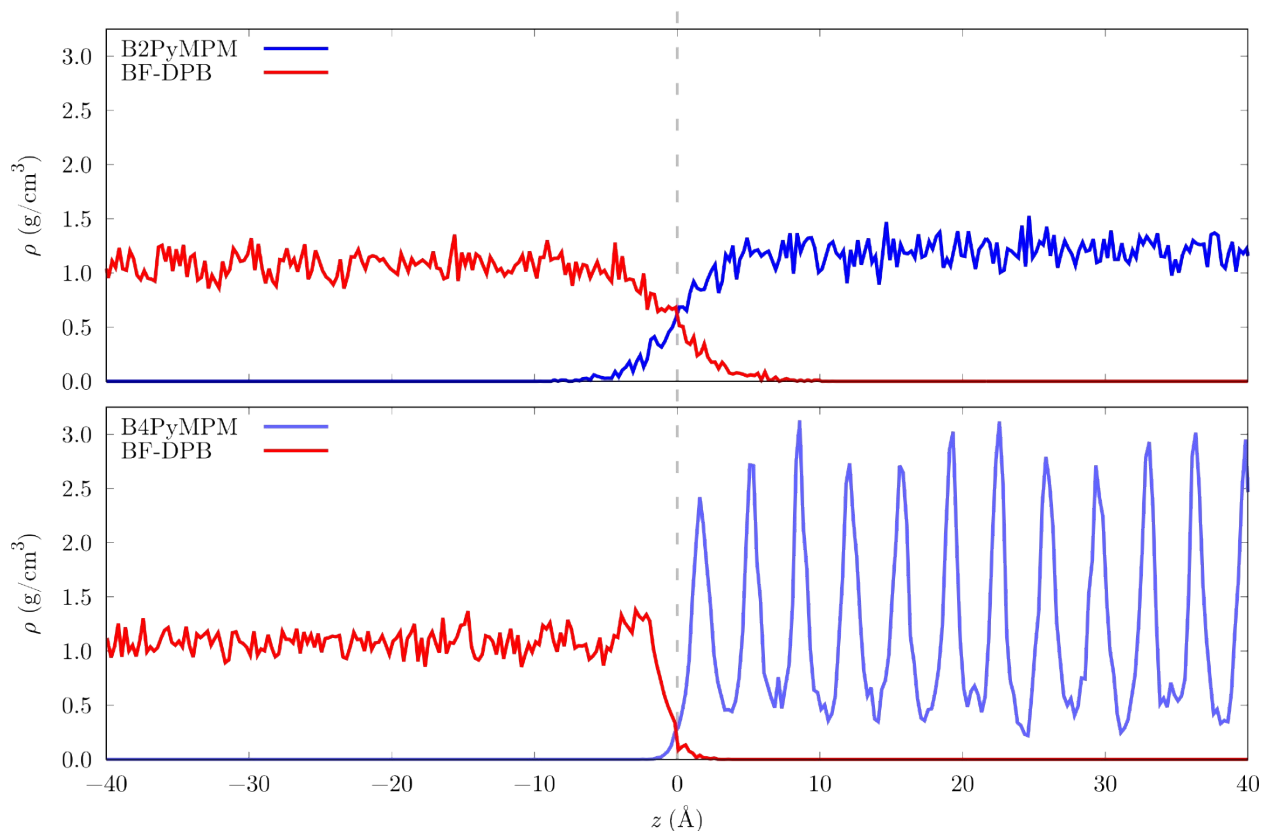

Figure S 18 Sample density (ρ) as a function af the z coordinate for the BF-DPB:B2PYMPM (top) and the BF-DPB:B4PYMPM (bottom) sample.

6.2. Parametrization and solution of the tight-binding model Hamiltonian

Molecular geometries were then extracted from the last MD configuration and used to calculate the parameters for a model tight-binding (TB) Hamiltonian, which involves D:A states relevant for the CT delocalization. These parameters were assessed by means of quantum chemical electronic structure and microelectrostatic (ME) calculations performed on the MD sample, accounting for fluctuations of site energies (diagonal disorder) and electron transfer integrals (off-

diagonal disorder). The electronic Hamiltonian, represented on a diabatic basis of localized molecular sites, reads:

$$H^{(i)} = \sum_j \epsilon_j^{(i)} |\phi_j\rangle\langle\phi_j| + \sum_{j,j'} J_{jj'}^e |\phi_j\rangle\langle\phi_{j'}| \qquad 6.1$$

where the sums run over the acceptor molecules, assuming that the hole is fixed on the i-th donor molecule. In such a way, the hole is allowed to experience a finite number of available donor sites (88 for the BF-DPB:B2PYMPM sample and 68 for the BF-DPB:B4PYMPM one). In this Hamiltonian, ϵ_j are the site energies of electrostatically interacting CT states, $|\phi_j\rangle$ represents the j-th acceptor LUMO and $J_{jj'}^e$ are the electron (LUMO-LUMO) transfer integrals between acceptor dimers. Site energies $\epsilon_j^{(i)}$ were computed combining the donor ionization potential (IP), the acceptor electron affinity (EA) and the electrostatic Coulomb interaction between the two charged molecules at a distance r_{ij}:

$$\epsilon_j^{(i)} = IP^{(i)} - EA_j - \frac{1}{4\pi\varepsilon_0\varepsilon r_{ij}} \qquad 6.2$$

where ε_0 is the vacuum permittivity and ε is the macroscopic dielectric constant of the medium, which was set equal to 3, a typical value for organic semiconductors. Following the common perturbative treatment of intermolecular interactions in the solid-state,[13] single carrier energy levels of localized charged excitations (*i.e.*, holes on donor BF-DPB and electrons on acceptor B*n*PYMPM (where n = 2, 4)) were obtained as the sum of two contributions: an intramolecular one, assessed at the quantum chemical level, and an environmental one, computed here with classical ME calculations using the MESCal code.[14]

The intramolecular contribution was obtained by combining DFT and many-body *GW* calculations, the latter permitting to obtain accurate gas-phase IP and EA values. Gas-phase *GW* calculations were performed on optimized DFT molecular structures starting from PBE0 Kohn-Sham levels obtained with the ORCA 4.2 package.[15] A partial self-consistent scheme on the eigenvalues (ev*GW*) was exploited, along with Gaussian basis sets of the Dunning's correlation-consistent family (cc-pVXZ, where X = 2, 3) and extrapolation of quasi-particle energy levels to the complete basis set limit.[16] The ev*GW* calculations were performed with the FIESTA code. Then, for each molecule in the MD samples, energy deviations of IP and EA arising from geometric distortions were evaluated as total energy differences (ΔSCF calculations) between charged and neutral species obtained by at the DFT PBE0/6-311++G(d,p) level of theory. The final gas-phase IP and EA of individual molecules were obtained as a sum of the ev*GW* values at the optimized geometry and their deviation with respect to the same geometry calculated at DFT level:[17]

$$E(R_{MD}) = E^{GW}(R_X) + \left[E^{DFT}(R_{MD}) - E^{DFT}(R_X) \right]$$ 6.3

where R_{MD} labels the geometry of a given molecule in the MD sample and R_X is a reference DFT optimized geometry.

In order to obtain the contribution of surrounding molecules to ionization energies, ME calculations were parametrized with ESP atomic charges and polarizability tensor calculated at the DFT PBE0/6-311++G(d,p) level. ESP charges were computed for all molecules extracted from the last MD configuration, in neutral, positively (for BF-DPB) and negatively (for BnPYMPM) charged states. The polarizability tensors were calculated at optimized geometries, and the polarizability of charged species was set equal to that of neutral ones. The environmental contribution to site energies consists of an electrostatic and an induction term. The electrostatic contribution was obtained with ME calculations on a 2D-periodic D:A interface, accounting for interactions with periodic replicas in the slab plane up to a cutoff distance of 800 Å, ensuring converged electrostatic sums. In practice, molecules within ±~40 Å from the D:A interface were selected and the resulting thin film was considered for 2D slab periodic calculations (see Figure 5b in the main text). For the induction term, the self-consistent induction energies for holes and electrons were calculated by using the entire MD sample and taking spherical clusters of increasing radius centered at the molecule of interest, and then extrapolated to the infinite radius limit.[13]

Electron transfer integrals $J_{jj'}^e$ were computed at the DFT PBE0/def2-SVP level of theory for those BnPYMPM dimers present in the thin film using the dimer projection method (LUMO-LUMO couplings).[18] The pair selection was done by taking all dimers whose minimum atom-atom distance was found to be less than 5 Å, considering PBC along xy plane. Such calculations were performed using ORCA 4.2.

According to Hamiltonian (#), for every position of the hole at the interface with the acceptor we computed delocalized electronic states $|\psi_m\rangle$, that can be written as a linear combination of N basis molecular orbitals $|\phi_j\rangle$:

$$|\psi_m\rangle = \sum_{j=1}^{N} c_{mj} |\phi_j\rangle$$ 6.4

where $\sum_{j=1}^{N} c_{mj}^2 = 1$. In practice, we considered a hemisphere of radius d centered at the hole site (see Figure 5c in the main text) and include in the Hilbert space all the LUMOs of acceptor molecules within this region.

The participation ratio (PR) associated to $|\psi_m\rangle$

$$PR_m = \left(\sum_{j=1}^{N} c_{mj}^4 \right)^{-1} \qquad 6.5$$

quantifies the degree of delocalization of the m-th state. For a fully localized state, the PR is equal to 1, while for the limiting case of a fully delocalized state, the PR is equal to N. We remark that, in analogy with previous works,[19,20] the description of the PR is based on a mere electronic picture, as it neglects relaxation effects. Thus, the computed PR provides an upper limit to the CT state delocalization.

The centroid of the m-th state is defined as:

$$r_{e,m} = \sum_{j=1}^{N} c_{mj}^2 r_j \qquad 6.6$$

where r_j is the center of mass of the j-th molecule. Once r_e is known, then the electron-hole (eh) distance r_{eh} can be computed as a difference:

$$r_{eh,m}^{(i)} = r_{e,m} - r_h^{(i)} \qquad 6.7$$

with $r_h^{(i)}$ the center of mass of the i-th donor carrying the hole.

The probability density function Γ of a given variable X can be written as:

$$\Gamma(X) = \frac{1}{N} \frac{\Delta n(X)}{\Delta X} \qquad 6.8$$

where $n(X)$ is the cumulative number of states sorted by X and N is the total number of states. This was computed by binning along one or more variables. As an example, $\Gamma(r_{eh}, E)$ is the probability density as a function of the eh distance and the state energy:

$$\Gamma(r_{eh}, E) = \frac{1}{N} \frac{\Delta n\left(\left[r_{eh} - \frac{\Delta r_{eh}}{2}, r_{eh} + \frac{\Delta r_{eh}}{2} \right], \left[E - \frac{\Delta E}{2}, E + \frac{\Delta E}{2} \right] \right)}{\Delta r_{eh} \Delta E} \qquad 6.9$$

The probability density as a function of the state energy is called density of states (DOS).

6.3. Results

We begin our results analysis starting from the diagonal elements of the TB Hamiltonian, that is the site energies of the CT states included in the chosen basis function. From now on, for the sake of conciseness, we will refer to the donor BF-DPB as DPB, while the two acceptors will be expressed by B2P and B4P.

Table S8 reports the average IP of DPB molecules in direct contact with the B2P and B4P interface, and the average EA of the two acceptors. The IP and EA probability densities are also shown in **Figure S 20**. If DPB molecules present the same IP distributions in gas-phase, environmental effects due to long-range intermolecular electrostatic interactions play a not negligible role at the solid-state. Indeed, we observe a difference of ~0.2 eV in the average IP of DPB as a result of the different molecular packing of the acceptor phase (*i.e.*, amorphous in B2P versus crystalline in B4P).

Table S8. Average IP for DPB molecules close to the interface and average EA for B2P and B4P, along with their respective standard deviations (in eV). Both gas-phase (gas) and solid-state (ss) values, upon accounting for environmental effects, are reported.

	IP (eV)	σ (eV)		EA (eV)	σ (eV)
DPB:B2P (gas)	6.49	0.13	B2P (gas)	0.82	0.09
DPB:B2P (ss)	5.61	0.19	B2P (ss)	1.42	0.22
DPB:B4P (gas)	6.49	0.09	B4P (gas)	1.32	0.08
DPB:B4P (ss)	5.82	0.13	B4P (ss)	2.01	0.11

Conversely, the difference in the gas-phase EA of the two acceptors (ev*GW* pointed to 0.5 eV energy difference) mainly lies in the position of the aryl nitrogen atoms, in *ortho*-position for B2P and in *para*-position for B4P, affecting the dihedral angles of the phenyl-phenyl groups (see **Figure S 19**). Besides, the morphological disorder of the acceptor phases is also reflected in the different broadening of EA distributions: the standard deviation σ of the B2P EA in the solid-state is twice as much that of the B4P EA, indicating a more ordered B4P material.
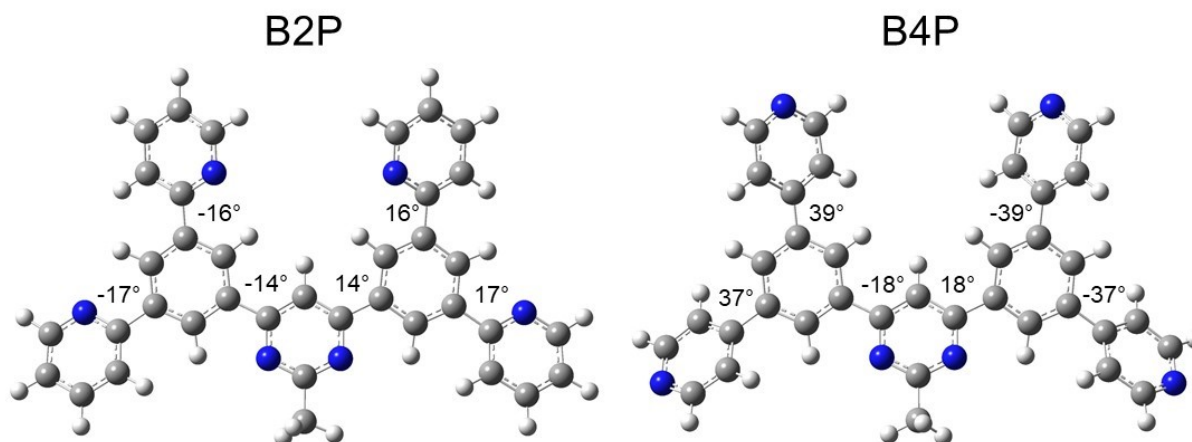

Figure S 19 Molecular geometry of the two acceptors, where the dihedral angle values are shown, as obtained by a ground-state DFT optimization at the B3LYP/6-31G(d) level.
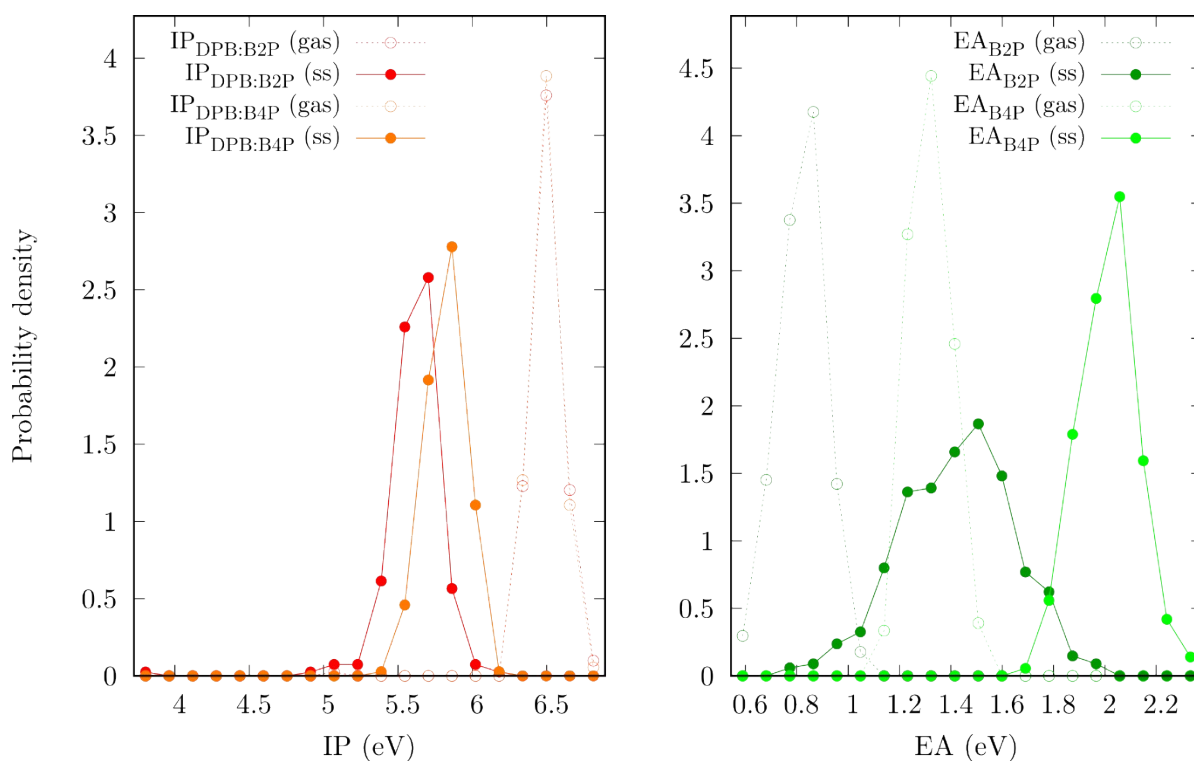
Figure S 20 Probability density as a function of the IP for DPB molecules (left) and the EA of the two acceptors (right), both in gas-phase (gas, dashed lines) and at the solid-state (ss, solid lines).

In addition, **Figure S 21** reports the evolution of the donor IP and the acceptor EA as a function of the z coordinate of the thin film extracted from the whole sample and comprising the heterointerface (represented with a black dotted line). The averaged profiles are rather flat, and we do not observe any band bending effect that would drives charge carriers away from the interface. We note that electrostatic *push-out* forces should bring electrons towards acceptor regions in the sample with higher EAs and, at the same time, holes towards donor regions with lower IPs. However, this is not the case and electrostatics is not the main responsible for the higher charge generation efficiency of B4P-based blends with respect to those based on B2P.
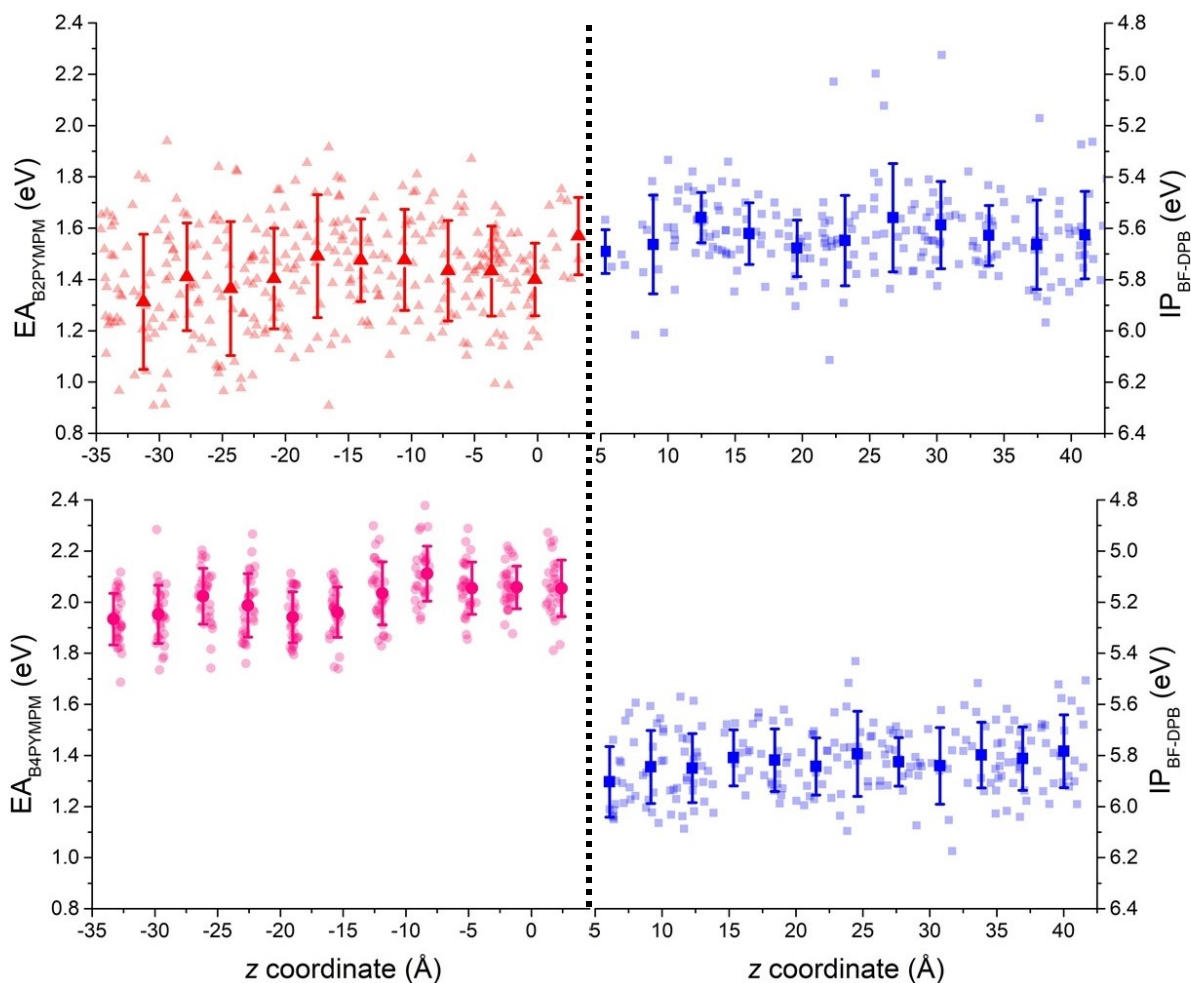
Figure S 21 Evolution of the donor IP (on the right) and the acceptor EA (on the left) as a function of the *z* coordinate of the thin film, where the black dotted line indicates the position of the interface. Average values with their standard deviations are reported, along with scattered raw data on the background. On top is shown the B2P:DPB sample, while on bottom the B4P:DPB one. Note that the energy scale of the IP goes from 6.4 to 4.8 eV, while that of the EA goes from 0.8 to 2.4 eV.

Regarding the off-diagonal elements of the TB Hamiltonian, that is the electronic transfer integrals $J_{jj'}^{e}$, **Figure S 22** shows the cumulative electronic connectivity of B2P and B4P as a function of the transfer integral module. The electronic connectivity represents the average number of neighbors that is connected to each molecule by a transfer integral exceeding a given value. Due to the different molecular arrangement, acceptor molecules in the crystalline B4P phase, forming 1D π-stacked columns, are better connected than those in the B2P amorphous phase.
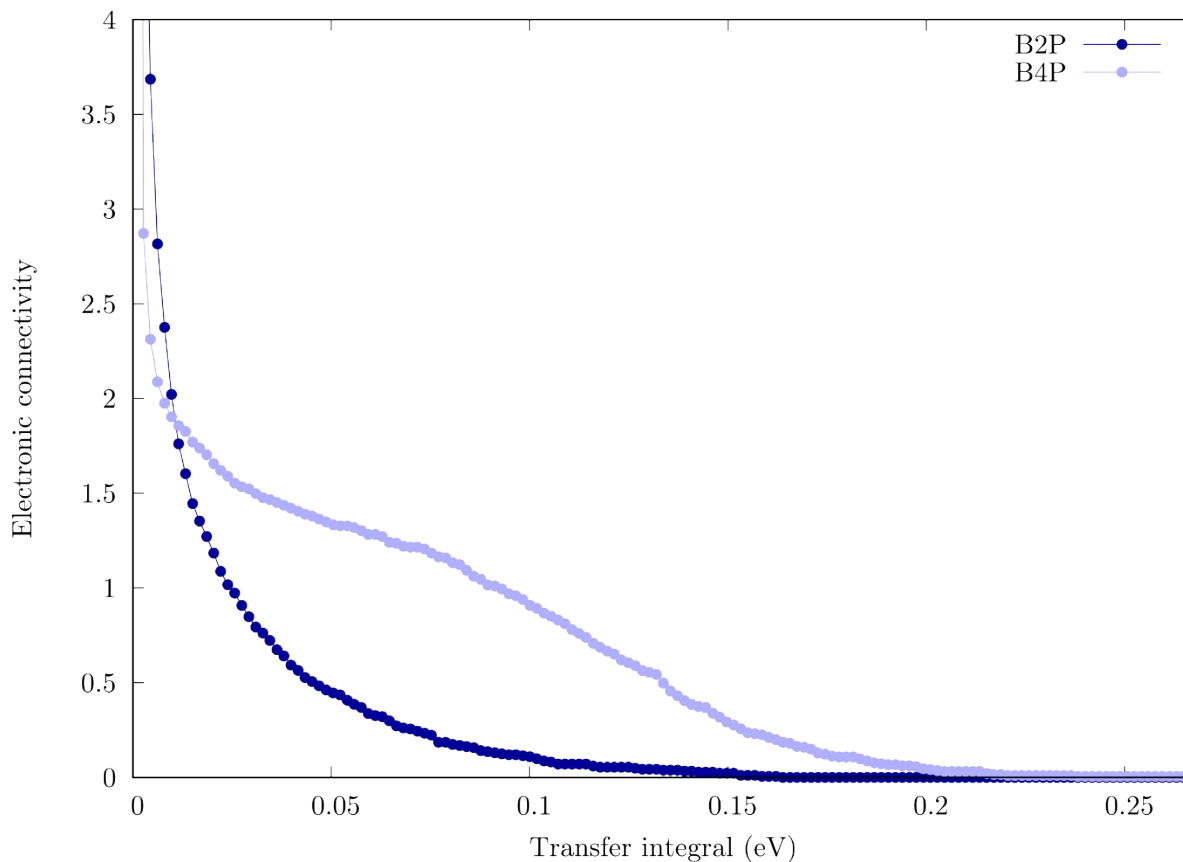
Figure S 22 Cumulative electronic connectivity as a function of the transfer integral module.

Figure S 23 shows the probability density as a function of r_{eh} and the state energy, a result of the resolution of the TB Hamiltonian of the two investigated systems by using hemispheres with a cutoff distance d of 60 Å. The two DOS $\Gamma(E)$ can also be seen as the energy distributions of the delocalized CT states in our basis functions and their mean value differs of ~0.4 eV. Moreover, the B2P DOS is slightly broader with respect to the B4P one. This is ascribable to a larger energetic disorder in the site energies (*i.e.*, in the diagonal disorder σ of the Hamiltonian, see Table S8).
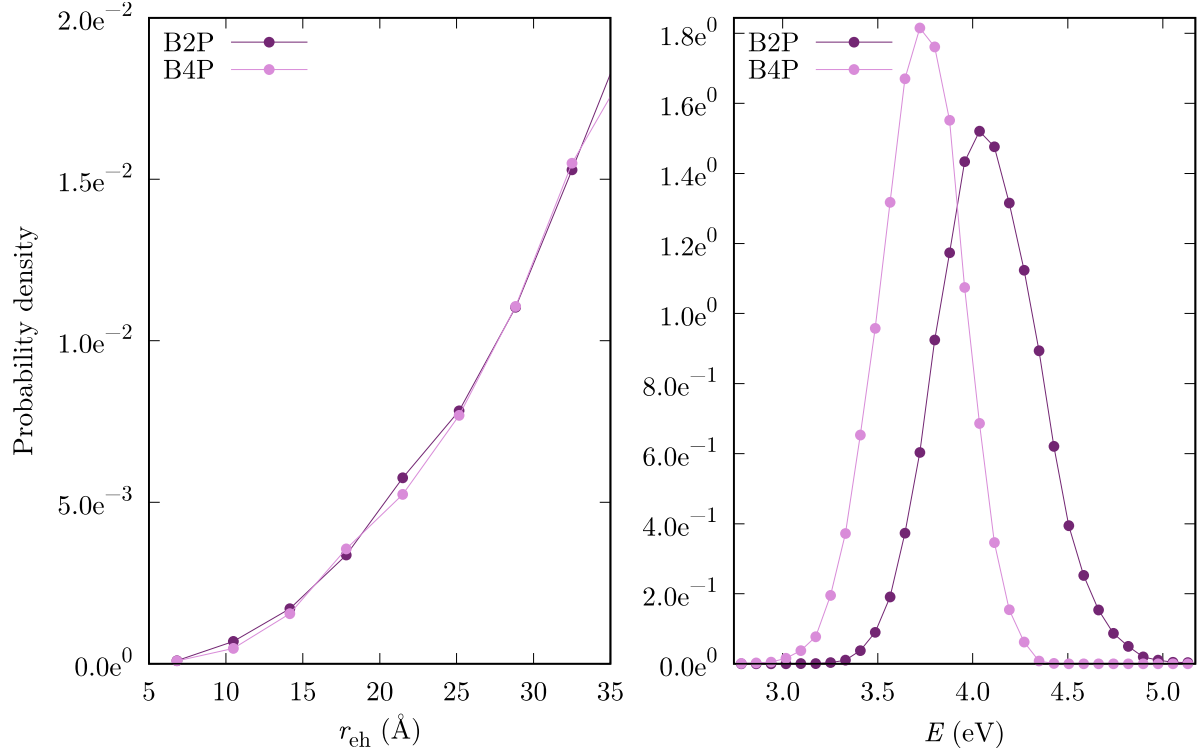
Figure S 23 Probability density as a function of the electron-hole distance r_{eh} (on the left) and of the state energy (on the right) for the DPB:B2P (purple) and DPB:B4P (light purple) system, using hemispheres with a cutoff distance d of 60 Å.

In the NVT canonical ensemble, the entropy S of a given system at a given temperature T reads:

$$S = k_B \ln Q + \frac{\langle E \rangle}{T} \qquad 6.\,10$$

where k_B is the Boltzmann constant, $Q \equiv \sum_m e^{-\frac{E_m}{k_B T}}$ is the partition function, with the index m running over the states, and $\langle E \rangle$ is the Boltzmann weighted average potential energy:[21]

$$\langle E \rangle = \frac{1}{Q} \sum_m E_m e^{-\frac{E_m}{k_B T}} \qquad 6.\,11$$

By dividing the system in spherical shells of thickness Δr, internal radius $r - \Delta r/2$ and external radius $r + \Delta r/2$, the entropy of the n-th shell with an average radius r_n can be written as:

$$S(r_n) = k_B \ln Q(r_n) + \frac{\langle E(r_n) \rangle}{T} \qquad 6.\,12$$

The Helmholtz free energy (A) of the two systems, DPB:B2P and DPB:B4P, defined as:

$$A \equiv E - TS = -k_B T \ln Q \qquad\qquad\qquad 6. \ 13$$

is shown in **Figure S 24** as a function of $r_n \equiv r_{eh}$ at 300 K, along with potential energy E and entropy S profiles in the case of localized and delocalized states (all energetic profiles were normalized with respect to the interface values). In general, the entropic term, similar in the two systems, is much smaller than the potential energy one. Consequently, the Helmholtz free energy and the potential energy profile are almost identical. Moreover, the DPB:B2P system exhibits an activation energy of 0.1-0.2 eV, while the DPB:B4P one shows an almost barrierless profile, even though with a positive slope, in **Figure S 24**a, while in **Figure S 24**b, by excluding the spike due to poor statistics in that region (as discussed in the main text), a 0.10-0.15 eV barrier is observed.
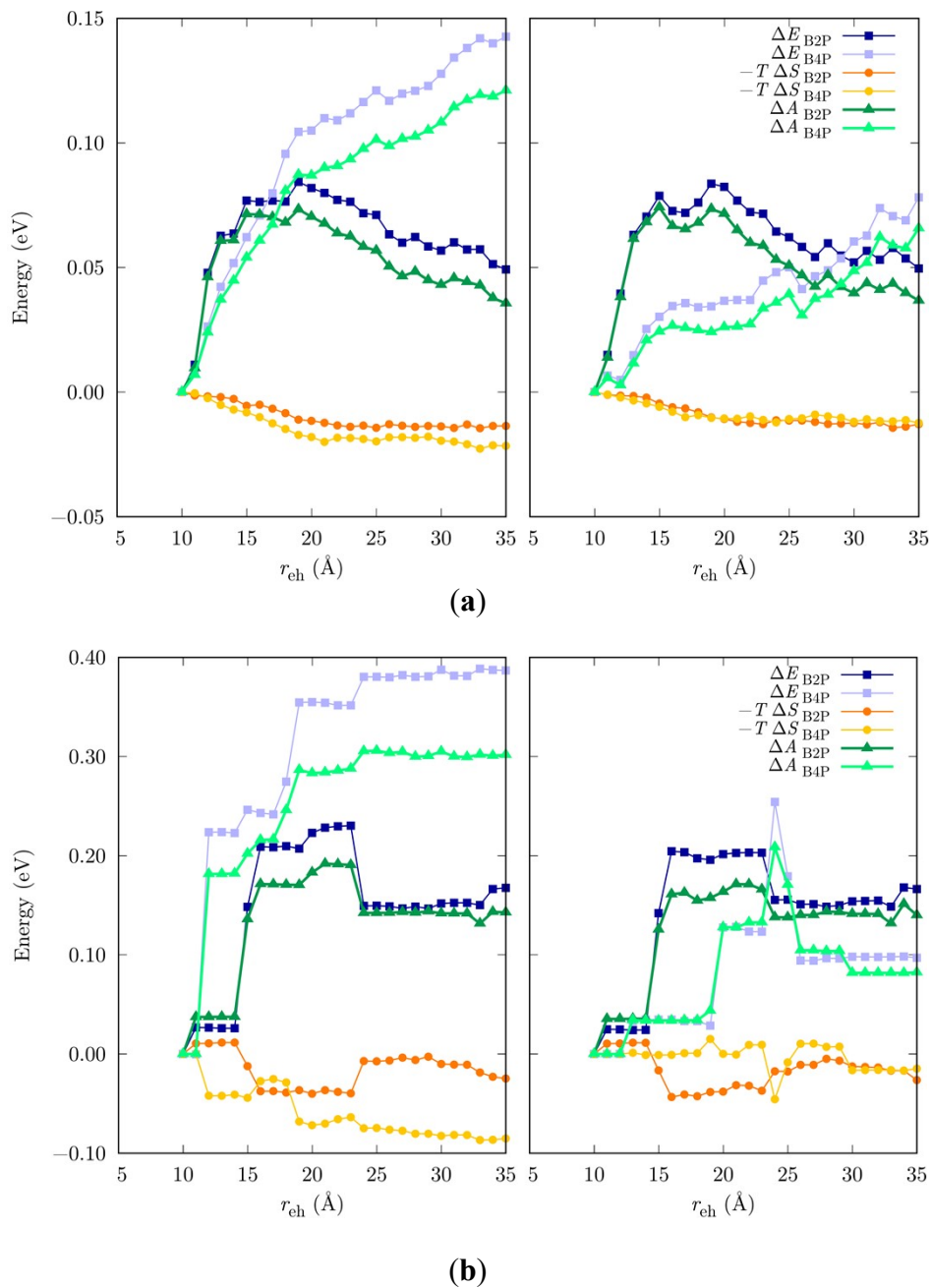
(a)

(b)

Figure S 24 Potential energy (ΔE), entropic contribution ($-T\Delta S$) and Helmholtz free energy (ΔA) at $T = 300$ K, normalized with respect to the interface values, as a function of the electron-hole distance r_{eh}. Left: localized charged states; right: delocalized charged states. a) Boltzmann-weighted average at 300 K obtained by treating each hole position as a separate system; b) Boltzmann-weighted average at 300 K obtained by considering all the states as belonging to a single system, regardless of the hole position.

The spread (σ) of the states along x, y and z is equal to the standard deviation of the position of the molecules involved in a delocalized state, weighted by their squared participation coefficient c_{mj}^2. For instance, the average spread z component associated to the delocalized state m:

$$\sigma_{z,m} \equiv \sqrt{\sum_j c_{mj}^2 (r_{ez,m} - r_{z,j})^2}$$

6. 14

gives the average quadratic displacement of the state along the coordinate perpendicular to the interface. Conversely, the module of the x and y components:

$$\sigma_{xy,m} \equiv \sqrt{\sigma_{x,m}^2 + \sigma_{y,m}^2}$$

6. 15

provides information about the displacement on the plane parallel to the interface. The mean spread perpendicular ($\sigma_\perp$) and parallel ($\sigma_\parallel$) components with respect to the interface are obtained by averaging the spread z and xy components over all the delocalized states, by means of either an arithmetic average:

$$\sigma_\perp \equiv \frac{1}{N} \sum_m \sigma_{z,m}$$

6. 16

$$\sigma_\parallel \equiv \frac{1}{N} \sum_m \sigma_{xy,m}$$

6. 17

or a Boltzmann average (at 300 K):

$$\sigma_\perp \equiv \frac{1}{Q} \sum_m \sigma_{z,m} e^{-\frac{E_m}{k_B T}}$$

6. 18

$$\sigma_\parallel \equiv \frac{1}{Q} \sum_m \sigma_{xy,m} e^{-\frac{E_m}{k_B T}}$$

6. 19

Table S9. Average spatial spread (σ) of delocalized states: arithmetic (A) and Boltzmann (B) averages in the DPB:B2P and DPB:B4P samples and its perpendicular ($\sigma_\perp$) and parallel ($\sigma_\parallel$) components with respect to the interface.

Sample		σ (Å)	$\sigma_\perp$ (Å)	$\sigma_\parallel$ (Å)
DPB:B2P	A	3.5	1.6	2.9
	B	0.3	0.2	0.2
DPB:B4P	A	3.9	3.0	2.4
	B	2.8	2.8	0.9

References

[1] C. Wu, P. I. Djurovich, M. E. Thompson, *Adv. Funct. Mater.* **2009**, *19*, 3157.

[2] Y. Shirota, Y. Kuwabara, H. Inada, T. Wakimoto, H. Nakada, Y. Yonemoto, S. Kawami, K. Imai, *Appl. Phys. Lett.* **1994**, *65*, 807.

[3] C. Murawski, C. Fuchs, S. Hofmann, K. Leo, M. C. Gather, *Appl. Phys. Lett.* **2014**, *105*, 113303.

[4] S. H. Hwang, Y. K. Kim, Y. Kwak, C. H. Lee, J. Lee, S. Kim, *Synth. Met.* **2009**, *159*, 2578.

[5] I. G. Hill, D. Milliron, J. Schwartz, A. Kahn, *Appl. Surf. Sci.* **2000**, *166*, 354.

[6] H. Sasabe, D. Tanaka, D. Yokoyama, T. Chiba, Y.-J. Pu, K. Nakayama, M. Yokoyama, J. Kido, *Adv. Funct. Mater.* **2011**, *21*, 336.

[7] K. Vandewal, *Annu. Rev. Phys. Chem.* **2016**, *67*, 113.

[8] J. Wang, R. M. Wolf, J. W. Caldwell, P. A. Kollman, D. A. Case, *J. Comput. Chem.* **2004**, *25*, 1157.

[9] M. J. Frisch, G. W. Trucks, H. B. Schlegel, G. E. Scuseria, M. A. Robb, J. R. Cheeseman, G. Scalmani, V. Barone, G. A. Petersson, H. Nakatsuji, X. Li, M. Caricato, A. V Marenich, J. Bloino, B. G. Janesko, R. Gomperts, B. Mennucci, H. P. Hratchian, J. V Ortiz, A. F. Izmaylov, J. L. Sonnenberg, D. Williams-Young, F. Ding, F. Lipparini, F. Egidi, J. Goings, B. Peng, A. Petrone, T. Henderson, D. Ranasinghe, V. G. Zakrzewski, J. Gao, N. Rega, G. Zheng, W. Liang, M. Hada, M. Ehara, K. Toyota, R. Fukuda, J. Hasegawa, M. Ishida, T. Nakajima, Y. Honda, O. Kitao, H. Nakai, T. Vreven, K. Throssell, J. A. Montgomery Jr., J. E. Peralta, F. Ogliaro, M. J. Bearpark, J. J. Heyd, E. N. Brothers, K. N. Kudin, V. N. Staroverov, T. A. Keith, R. Kobayashi, J. Normand, K. Raghavachari, A. P. Rendell, J. C. Burant, S. S. Iyengar, J. Tomasi, M. Cossi, J. M. Millam, M. Klene, C. Adamo, R. Cammi, J. W. Ochterski, R. L. Martin, K. Morokuma, O. Farkas, J. B. Foresman, D. J. Fox, **2016**.

[10] Y. Watanabe, H. Sasabe, D. Yokoyama, T. Beppu, H. Katagiri, Y.-J. Pu, J. Kido, *Adv. Opt. Mater.* **2015**, *3*, 769.

[11] J. C. Phillips, R. Braun, W. Wang, J. Gumbart, E. Tajkhorshid, E. Villa, C. Chipot, R. D. Skeel, L. Kalé, K. Schulten, *J. Comput. Chem.* **2005**, *26*, 1781.

[12] L. Muccioli, G. D'Avino, R. Berardi, S. Orlandi, A. Pizzirusso, M. Ricci, O. M. Roscioni, C. Zannoni, *Top. Curr. Chem.* **2013**, *352*, 39.

[13] G. D'Avino, L. Muccioli, F. Castet, C. Poelking, D. Andrienko, Z. G. Soos, J. Cornil, D. Beljonne, *J. Phys. Condens. Matter* **2016**, *28*, 433002.

[14] G. D'Avino, L. Muccioli, C. Zannoni, D. Beljonne, Z. G. Soos, *J. Chem. Theory Comput.* **2014**, *10*.

[15] F. Neese, *WIREs Comput. Mol. Sci.* **2018**, *8*.

[16] J. Li, I. Duchemin, O. M. Roscioni, P. Friederich, M. Anderson, E. Da Como, G. Kociok-Köhn, W. Wenzel, C. Zannoni, D. Beljonne, X. Blase, G. D'Avino, *Mater. Horizons* **2019**, *6*, 107.

[17] G. Londi, S.-U.-Z. Khan, L. Muccioli, G. D'Avino, B. P. Rand, D. Beljonne, *J. Phys. Chem. Lett.* **2020**, *11*, 10219.

[18] B. Baumeier, J. Kirkpatrick, D. Andrienko, *Phys. Chem. Chem. Phys.* **2010**, *12*, 11103.

[19] G. D'Avino, Y. Olivier, L. Muccioli, D. Beljonne, *J. Mater. Chem. C* **2016**, *4*, 3747.

[20] G. D'Avino, L. Muccioli, Y. Olivier, D. Beljonne, *J. Phys. Chem. Lett.* **2016**, *7*, 536.

[21] S. N. Hood, I. Kassal, *J. Phys. Chem. Lett.* **2016**, *7*, 4495.